13 (2026) 97–123

Contents lists available at ScienceDirect

Computational Particle Mechanics

journal homepage: www.sciencedirect.com/journal/computational-particle-mechanics

Coupling of SPH and Volume-of-Fluid for multiphase flow☆

Markus Wicker *, Niklas Bürkle, Rainer Koch, Hans-Jörg Bauer

Institute of Thermal Turbomachinery, Karlsruhe Institute of Technology (KIT), Karlsruhe, Germany

ARTICLE INFO

Keywords:
Smoothed Particle Hydrodynamics (SPH)
Volume-of-Fluid (VoF)
SPH–FV coupling
Domain decomposition
Multiphase flow
Surface tension

ABSTRACT

A new methodology for coupling Smoothed Particle Hydrodynamics (SPH) with a Finite Volume (FV) solver for multiphase flow is presented. The approach follows a patched-domain strategy in which the two domains are disjointly separated by a discrete coupled boundary. Consequently, the coupled SPH–FV method is able to benefit from both methods' strengths in their respective domains. The SPH solver employs a custom scheme, whereas a preexisting FV solver employing a Volume-of-Fluid (VoF) multiphase representation is adapted with minor modifications.

Key features of the coupling include the determination of the volume fraction at the coupled boundary, the preservation of the fluid interface, and surface tension modeling in the vicinity of the coupled boundary. The method is validated against a series of benchmark cases, showing very good agreement. To our knowledge, this is the first coupled SPH–FV method that allows interface advection across the coupled boundary for multiphase flow with surface tension.

1. Introduction

In multiphase flows, particularly those with chaotic interface fragmentation, such as atomization, SPH is commonly used due to its inherent interface capturing and associated high performance. Far from the interface, however, the use of grid-based methods such as Finite-Volume (FV) methods is often preferable over SPH due to their higher maturity, e.g. in terms of variable spatial resolution and boundary conditions. Consequently, a coupled approach, in which a SPH domain, confined to the region of interface fragmentation, is embedded into a surrounding FV domain, appears desirable, as this would take advantage of both methods' strengths.

Although in an application such as atomization the interface fragmentation may occur in a specific region, the resulting fragments can and will be advected away from the fragmentation region. Therefore, a coupled SPH–FV approach must allow for interface advection over the coupled boundary.

Existing coupling approaches between SPH and Finite-Volume (FV) methods can be classified by their domain decomposition strategy [1] as illustrated in Fig. 1: patched, overlapping, and zonal domains. Patched domains feature coinciding boundaries, resulting in a discrete coupled boundary. Conversely, if the boundaries of the two domains do not coincide, both solutions coexist in the overlap. Finally, in a zonal approach, one domain encompasses the global domain, while the other is limited to a subset.

Marrone et al. [2] developed an overlapping approach based on the previous work by Bouscasse et al. [3], where the SPH domain encompasses the free surface region, while an FV solver is used to simulate the fluid far from the free surface. In the overlap of the two domains, a blending procedure is applied. This approach was extended through the coupling of SPH with a Level-Set method to allow interface advection over the coupled boundary [4] and to enable application to three-dimensional cases [5]. Di Mascio et al. [5] also included an investigation of a zonal configuration in which the FV domain encompasses the whole domain. In the

☆ This article is part of a Special issue entitled: 'CPMS_SPHERIC' published in Computational Particle Mechanics.

* Corresponding author.
E-mail address: markus.wicker@kit.edu (M. Wicker).

https://doi.org/10.1016/j.cpms.2025.12.001
Received 21 August 2025; Received in revised form 23 December 2025; Accepted 24 December 2025

Available online 29 December 2025

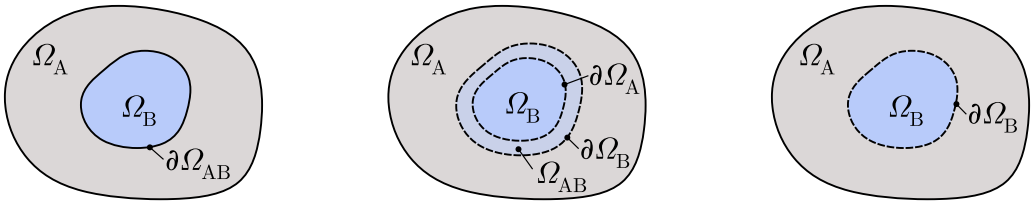

(a) Patched domains (b) Overlapping domains (c) Zonal domains

Fig. 1. Domain decomposition strategies.

SPH domain, that is limited to a subset of the FV domain, the FV solution is forced by the SPH solution. Li et al. [6] adapted the approach from Ref. [2] to provide improved boundary conditions for SPH simulations of compressible bubble dynamics.

Xu et al. developed [7] and subsequently improved [8–10] on a zonal coupling approach for multiphase flow, in which one fluid is discretized using SPH particles that are used to advect the fluid interface and compute interfacial forces. Another zonal approach presented by Myers et al. [11] employs a more finely resolved SPH domain within a more coarsely resolved FV domain to compute the flow in the vicinity of a shock.

In contrast to these overlapping and zonal approaches, Napoli et al. [12] proposed a patched configuration in which the SPH and FV domains are disjointly separated by a discrete interface. Both domains are extended by an *interface* region, in which the state of the cells/particles are obtained iteratively through interpolation from the other domain. Werdelmann et al. [13] developed a new permeable boundary condition and employed it in a patched coupling procedure in which only the SPH domain is extended by a *ghost particle* domain. While the coupled boundary conditions are imposed on the SPH domain using these *ghost particles*, they are directly imposed on the FV domain at the cell faces that coincide with the coupled boundary.

Apart from the zonal coupling configuration tested by Di Mascio et al. [5] who state their motivation as simplicity at a cost of a small overhead, other zonal approaches [7,11] combine FV and SPH rather than purely taking advantage of each method's strengths in their respective regions, as we intend to do. Therefore, we deem a zonal approach to be less suitable for our purposes.

However, irrespective of the domain decomposition strategy, the algorithm for the generation/elimination of particle mass is crucial to allow for mass flux over the coupled boundary. Chiron et al. [4] employ a modified version of the open boundary condition from Kassiotis et al. [14], applied at the outside of the overlap region. To ensure a regular particle distribution in the overlap, a shifting velocity adapted from Oger et al. [15] is applied. The drawback of this approach is that the mass fluxes into and out of the two domains are not imposed at coinciding locations, and hence, ensuring optimal mass conservation is difficult. The approach proposed by Napoli et al. [12] relies on a *mirror particle* procedure at the interface. Although this approach features a distinct coupling interface, the mass flux in and out of the FV domain is not imposed directly at this interface but rather implicitly through interpolation of the flow at the *interface cell* centers. Consequently, matching mass fluxes are not guaranteed. The coupling approach by Werdelmann et al. [13] in contrast features a mass generation/elimination algorithm that is designed to match the mass flux into and out of both domains over the coupled boundary, thus optimizing mass conservation both locally and globally. Additionally, as the coupling conditions are imposed on the FV domain on the boundary faces in a FV-typical fashion, their approach can be implemented with only minor modifications to an existing FV solver. In our opinion, these aspects constitute a significant conceptual advantage.

The aim of this article is to present a coupled SPH–FV method for multiphase flow in which the global domain can be decomposed into SPH and FV regions according to the respective strengths of both methods. For future applications including interface fragmentation, such as atomization, the coupled method must permit advection of the fluid interface over the coupled boundary. Although such coupled SPH–FV approaches for free surface flow can be found in the literature [4,5], there are, to our knowledge, no existing coupling methods for multiphase flow, including surface tension, that satisfy this requirement. Therefore, building on the work by Werdelmann et al. [13], we propose a novel coupling methodology in which the Volume-of-Fluid (VoF) method serves as a multiphase representation in the FV domain.

The paper is organized as follows: The employed numerical methods are reviewed in Section 2. Section 3 details the coupling procedure, with emphasis on multiphase aspects. Section 4 presents the validation of the coupling through test cases addressing relevant physical phenomena. Conclusions and prospects for future work are given in the final section.

2. Numerical methods

In this section, the numerical methods employed in the coupled SPH–VoF framework are described. The SPH domain is solved using a custom weakly compressible SPH (WCSPH) scheme, while the VoF solver is based on an existing open-source implementation with minor modifications.

In both domains, fluids are modeled as weakly-compressible with the barotropic equation of state

$$p = \frac{\rho_0 c^2}{\gamma}\left[\left(\frac{\rho}{\rho_0}\right)^{\gamma} - 1\right] . \tag{1}$$

Pressure, barotropic exponent, speed of sound are denoted as p, γ and c respectively, while ρ and ρ_0 indicate the fluid and reference density.

2.1. Smoothed particle hydrodynamics

The SPH solver employs a transport-velocity formulation similar to that proposed by Werdelmann et al. [13]. In this scheme, the particles are advected with a transport velocity $\vec{\tilde{u}}_i$ consisting of the fluid velocity $\vec{u}_i$ and the shifting velocity $\vec{\delta u}_i$:

$$\frac{d\vec{x}_i}{dt} = \vec{\tilde{u}}_i = \vec{u}_i + \vec{\delta u}_i. \tag{2}$$

Fluid density and velocity are evolved according to

$$\frac{d\rho_i}{dt} = -\rho_i \sum_j V_j(\vec{u}_j - \vec{u}_i)\cdot\vec{\nabla}W_{ij} + \vec{\delta u}_i \cdot \sum_{j\in\chi_i} V_j(\rho_j - \rho_i)\vec{\nabla}W_{ij} + \delta h_\sigma D_i^\rho \,, \tag{3}$$

$$\frac{d\vec{u}_i}{dt} = \vec{\delta u}_i \cdot \sum_j V_j(\vec{u}_j - \vec{u}_i)\otimes\vec{\nabla}W_{ij} + \vec{a}_i^p + \vec{a}_i^\tau + \vec{a}_i^\sigma + \vec{f}_i. \tag{4}$$

The mass of a particle m_i is kept constant within the domain and the particle volume is evaluated as $V_i = m_i/\rho_i$. Of particular note are the second term on the RHS of (3) and the first in (4), which represent the correction terms of fluid density and velocity due to the shifting velocity. The last term in (3) is the density diffusion term as proposed by Ferrari et al. [16], scaled not with the 'geometrical' smoothing length h, but rather based on the kernel's standard deviation σ with $h_\sigma = 2\sigma$ [17], as well as the numerical parameter $\delta = 0.1$. The density correction term as well as the density diffusion term is only computed over the neighbors j belonging to the same fluid χ as particle i.

The acceleration due to the pressure gradient, $\vec{a}_i^p$, is computed using the tensile instability control switch by Sun et al. [18], modified to include all particles within a distance of the kernel radius H of the coupled boundary $\partial\Omega$:

$$\vec{a}_i^p = \begin{cases} -\frac{1}{\rho_i}\sum_j V_j(p_i + p_j)\vec{\nabla}W_{ij}, & p_i \geq 0 \wedge \|x - \partial\Omega\| > H \\ -\frac{1}{\rho_i}\sum_j V_j(p_j - p_i)\vec{\nabla}W_{ij}, & p_i < 0 \vee \|x - \partial\Omega\| \leq H \end{cases} \tag{5}$$

The acceleration due to viscous forces, $\vec{a}_i^\tau$, is computed using the formulation of Szewc et al. [19] as

$$\vec{a}_i^\tau = \sum_j 2m_j(d+2)\frac{\nu_i + \nu_j}{\rho_i + \rho_j}\frac{(\vec{u}_i - \vec{u}_j)\cdot\vec{x}_{ij}}{x_{ij}^2 + \eta^2}\vec{\nabla}W_{ij} \,. \tag{6}$$

Here, ν denotes the kinematic viscosity, d the number of dimensions which in this work is limited to 2, and $n = 0.01/h$ is a numerical parameter to avoid instabilities for very small distances $x_{ij} = \|\vec{x}_{ij}\| = \|\vec{x}_i - \vec{x}_j\|$ between particles. The acceleration due to surface tension, $\vec{a}_i^\sigma$, is calculated using a modified version of the Continuum Surface Force (CSF) [20] formulation by Adami et al. [21]:

$$\vec{a}_i^\sigma = -\frac{1}{\rho}\sigma\kappa_i\vec{\hat{n}}_i\|\vec{\nabla}\alpha_i\| \,, \tag{7}$$

$$\vec{\nabla}\alpha_i = \frac{1}{V_i}\sum_j f_{ij}^\sigma\vec{\nabla}W_{ij} \,, \tag{8}$$

$$\vec{\hat{n}}_i = \frac{\vec{\nabla}\alpha_i}{\|\vec{\nabla}\alpha_i\|} \,, \tag{9}$$

$$\kappa_i = -d\frac{\sum_j V_j\left(\vec{\hat{n}}_i - \vec{\hat{n}}_j\right)\cdot\vec{\nabla}W_{ij}}{\sum x_{ij}V_j\vec{\nabla}W_{ij}} \,. \tag{10}$$

The interface normal vector $\vec{\hat{n}}$ and the curvature κ are computed analogously to the work of Adami et al. while the factor f_{ij}^σ in the gradient approximation of the volume fraction $\vec{\nabla}\alpha$ differs from Ref. [21], as will be explained in Section 3.4. It should be noted, that although Adami et al. follow the terminology of Brackbill et al. [20] of a color function instead of a volume fraction, both terms can be used interchangeably in this context.

Finally, $\vec{f}_i$ represents the acceleration due to a body force such as gravity.

The shifting velocity is derived from the particle shifting technique presented by Lind et al. [22], augmented by an additional repulsive interface force (RIF) [23], as

$$\vec{\delta u} = -D_i^\delta\frac{h_\sigma^2}{\Delta t}\left(\sum_j V_j\vec{\nabla}W_{ij} + \varepsilon_{\mathrm{RIF}}\sum_{j\notin\chi} V_j\vec{\nabla}W_{ij}\right). \tag{11}$$

Grenier et al. [23] introduce the RIF term in the momentum equation to prevent numerical dispersion of the fluid interface in the absence of surface tension. In the present scheme, the term is added to the shifting velocity to prevent perturbation of the fluid interface through shifting. As addressed in Bürkle et al. [24], the RIF term aims to counterbalance the interface-normal component of the first term in Eq. (11) implicitly. This differs from the common strategy of explicitly detecting the interface and eliminating the normal component (e.g. [22,25]). Grenier et al. [23] propose a parameter range of $0.01 \leq \varepsilon_{\mathrm{RIF}} \leq 0.1$, although for all cases presented in this work as well as those by Bürkle et al. [24], $\varepsilon_{\mathrm{RIF}}$ is set to 0.01, yielding good results. Nevertheless, the particle

shifting scheme and its impact on the fluid interface merit further investigation; however, this is beyond the scope of this current work. The variable D_i^δ can be described as the shifting diffusion coefficient and is set following Xenakis et al. [26] as

$$D_i^\delta = \max\left(\epsilon \frac{h_\sigma^2}{\Delta t}, A h_\sigma \|\vec{u}_i\|\right) \tag{12}$$

The parameter A is set to 2 throughout this work and ϵ is set case-dependent in the range $0.05 \leq \epsilon \leq 0.5$.

Time integration of Eqs. (2), (3) and (4) is performed using an explicit mid-point scheme:

$$\begin{aligned} \phi^{n+\frac{1}{2}} &= \phi^n + \frac{\Delta t}{2}\left(\frac{d\phi}{dt}\right)^n, \\ \phi^{n+1} &= \phi^n + \Delta t\left(\frac{d\phi}{dt}\right)^{n+\frac{1}{2}} \end{aligned} \tag{13}$$

Here, ϕ represents position $\vec{x}$, density ρ and velocity $\vec{u}$.

The time step size Δt is chosen to satisfy the criteria

$$\Delta t \leq C_\tau \min\left(\frac{h_\sigma^2 \rho_i}{\mu_i}\right), \tag{14}$$

$$\Delta t \leq C_a \min\left(\sqrt{\frac{h_\sigma}{\|\vec{a}_i\|}}\right), \tag{15}$$

$$\Delta t \leq C_c \min\left(\frac{h_\sigma}{c_i}\right), \tag{16}$$

$$\Delta t \leq C_\sigma \min\left(\sqrt{\frac{h_\sigma^3 \rho_i}{2\pi\sigma}}\right), \tag{17}$$

with the constants $C_\tau = 0.125$ and $C_a = C_c = C_\sigma = 0.25$.

Throughout this work, a Wendland C2 kernel is employed with a radius of $H = 4dx$.

2.2. Volume-of-fluid

The VoF solver is based on *compressibleInterFlow* from the *TwoPhaseFlow* package [27], an open-source extension to *OpenFOAM*. The solver is modified to employ the barotropic equation of state (1) and to omit the energy equation.

The interface is advected using the geometric *isoAdvector* approach [28] with a interface reconstruction based on a reconstructed distance function (RDF) $\boldsymbol{\Phi}$ [29]. Surface tension forces are computed through a CSF approach analogous to Eq. (7) with the curvature computation based on Cummins et al. [30]. In this implementation, the interface normal vector $\hat{n}$ is approximated as the gradient of the RDF:

$$\vec{n}_{\boldsymbol{\Phi}} = \frac{\vec{\nabla}\boldsymbol{\Phi}}{\|\vec{\nabla}\boldsymbol{\Phi}\|} \tag{18}$$

This interface normal vector is then interpolated from cell centers to face centers and from this the curvature κ is computed as

$$\kappa = \vec{\nabla} \cdot \vec{n}_{\boldsymbol{\Phi}}. \tag{19}$$

Time integration is performed through an implicit Euler scheme.

3. Coupling of SPH and VoF domain

As explained in Section 1, the proposed coupling approach follows the patched-domain strategy as illustrated in Fig. 2. The desired domain decomposition in an applied setting is highlighted through the example of a prefilming atomizer, a case to which SPH has been successfully applied [31]. In a hypothetical coupled SPH–VoF simulation, a cohesive film would be transported from the VoF domain Ω_{VoF} to the SPH domain Ω_{SPH}. Here, the film would be disintegrated into a disperse spray that is subsequently advected back into the VoF domain. Such a setup would be able to maintain the inherent advantages of SPH regarding interface fragmentation, while simultaneously benefiting from advanced features of FV methods such as more mature boundary conditions and variable spatial resolution.

The foundation of the coupled SPH–VoF method is the discrete coupling interface $\partial\Omega$ that separates the domains. This coupled boundary is decomposed into individual segments s with the area $A_s = dx^{d-1}$, where dx denotes the mean particle spacing and d the number of dimensions, which in this work is limited to 2. The SPH domain is additionally extended by Eulerian *ghost* particles located in the VoF domain, establishing full kernel support of the boundary. Flows with truncated kernel support, such as free-surface flows, are out of scope of the present work.

The coupling of the two domains is realized in a three-step procedure. First, the flow variables pressure p, velocity $\vec{u}$, and volume fraction α of the ghost particles $\mathcal{G}$ are determined by linear interpolation from the VoF solution. Afterwards the state of the individual segments of the boundary are determined from the information of both the regular SPH particles and the ghost particles. Finally, this state is communicated to the VoF solver as Dirichlet boundary conditions.

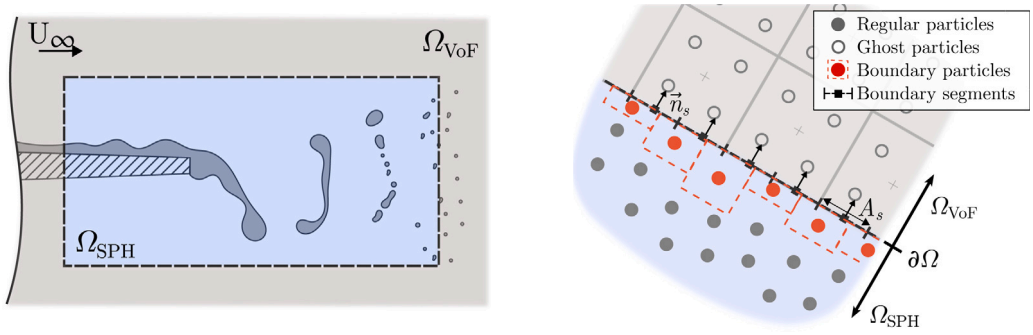

(a) Domain decomposition (b) Coupled boundary

Fig. 2. Schematic representation of the coupled SPH–VoF approach illustrate through the case of a prefilming atomizer.

One advantage of the proposed coupling method is that it can be implemented with only minor alterations to the VoF solver. Consequently, the following description of the coupling methodology constitutes modifications of the SPH solver unless otherwise stated.

3.1. Mass flux algorithm

Realizing a mass flux over the coupled boundary is trivial for FV methods but not for SPH. Werdelmann et al. [13] have developed a novel permeable boundary approach that does not rely on a buffer region but instead features an algorithm for the continuous mass flux across the boundary. Recently, Bürkle et al. [24] have employed this algorithm in a multi-resolution SPH framework for multiphase flow. In the following, we review the algorithm including some minor modifications, particularly in regards to a VoF-type representation of the boundary.

The total mass advected into the SPH domain over a boundary segment s in a time step $t \to t + \Delta t$ is given by

$$\Delta m_s = -\rho_s A_s \left(\vec{u}_s \cdot \vec{n}_s\right) \Delta t \,, \tag{20}$$

with $\vec{n}_s$ as the normal vector on s pointing from SPH into VoF domain. In a VoF-type approach, the advected mass belonging to fluid χ can be expressed using the volume fraction $\alpha_{s,\chi}$ of the segment as

$$\Delta m_{s,\chi} = -\alpha_{s,\chi} \rho_{s,\chi} A_s \left(\vec{u}_s \cdot \vec{n}_s\right) \Delta t \,. \tag{21}$$

Together with the equation of state (1), the relation between density, pressure and volume fraction is determined by

$$\rho_s = \alpha_s \rho_{s,1} + (1 - \alpha_s)\rho_{s,2} \,. \tag{22}$$

This mass flux is realized through an incremental increase or decrease of the mass of boundary particles $\mathcal{B}$ based on some simple geometric considerations as illustrated in Fig. 3: Particles are considered to be d-dimensional cuboids, characterized by a cross-sectional area $A_i = A_s \left(\rho_{i,\chi}/\rho_{0,\chi}\right)^{\frac{1-d}{d}}$ parallel, and an extent of $l_i = V_i/A_i$ perpendicular to the coupled boundary. If a cuboid is either in contact with the boundary at time t, or if it comes into contact during the time step $t \to t + \Delta t$ due to advection with the transport velocity $\vec{u}$, the particle is considered to be in the set of boundary particle $\mathcal{B}$ eligible for mass change. The particle mass advected over the boundary can then be predicted from the positions $\vec{x}$ of particle i and the closest boundary segment s as

$$\delta m_i^* = -\rho_i A_i \left[\left(\vec{\hat{u}}_i \cdot \vec{n}_s\right) \Delta t - \left(\vec{x}_{si} \cdot \vec{n}_s - \frac{l_i}{2}\right)^+\right] . \tag{23}$$

The second term in the brackets is modified by the superscript $(\cdot)^+ = \max(0, \cdot)$ as it is only relevant when the particle is not in contact with the boundary prior to advection. Note, that once a particle is in contact with the boundary, the shifting velocity component normal the boundary is set to zero and therefore $\vec{\hat{u}}_i \cdot \vec{n}_s = \vec{u}_i \cdot \vec{n}_s$. As a particle cannot possess a negative mass and should not have more than the nominal mass m_0, the mass change is limited to

$$0 \leq m_i + \delta m_i \leq m_0 = \rho_0 d x^d \,. \tag{24}$$

The predicted mass δm^* can be associated with a boundary segment based on their geometric overlap $\omega_{is} = \frac{A_i \cap A_s}{A_s}$. As a result, the imbalance of the prescribed mass Δm and predicted mass δm^* can be evaluated for each boundary segment and each fluid as

$$\mathcal{M}_{s,\chi} = \Delta m_{s,\chi} - \sum_{i \in \chi} \omega_{is} \delta m_i^* \,. \tag{25}$$

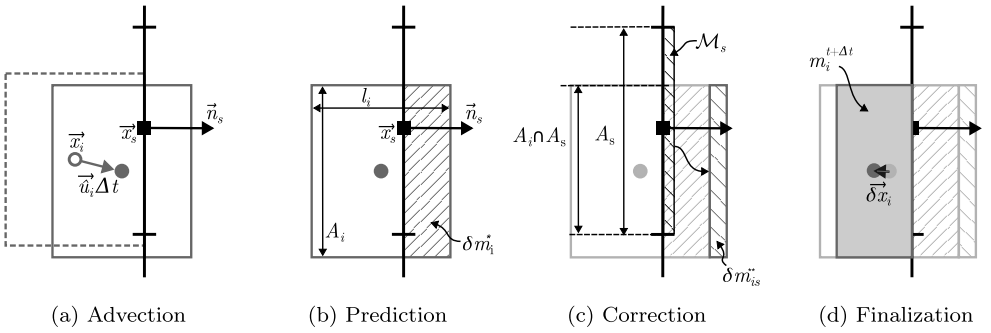

Fig. 3. Schematic representation of the mass flux algorithm, illustrating the steps for imposing an incremental mass change of a boundary particle.

In order to optimize local and global mass conservation, this imbalance $\mathcal{M}_{s,\chi}$ is compensated by imposing corrective mass increments δm_{is}^{**} so that

$$\mathcal{M}_{s,\chi} = \sum_{i \in \chi} \delta m_{is}^{**} \tag{26}$$

is satisfied.

In case of a negative imbalance $\mathcal{M}_{s,\chi} < 0$, additional particle mass has to be removed. For this, the closest boundary particle $i \in \mathcal{B}$ with $\omega_{is} > 0$ is selected. If, due to the limits in Eq. (24), the imbalance cannot be compensated, we iteratively continue with the other boundary particles with $\omega_{is} > 0$.

For a positive imbalance $\mathcal{M}_{s,\chi} > 0$ our approach differs slightly from Werdelmann et al. [13], as we first try to impose a corrective mass on the furthest particle with $\omega_{is} > 0.5$. Only if the imbalance cannot be compensated through corrective mass increments on particles with $\omega_{is} > 0.5$, we subsequently try the closest particle with $0.5 \geq \omega_{is} > 0$. If after this there is still a mass imbalance over a segment, a new particle of that mass is created, or if the imbalance is negative, it is stored for the next time iteration.

The new mass of a particle after the timestep $t \rightarrow t + \Delta t$ is then given by

$$m_i^{t+\Delta t} = m_i^t + \left(\delta m_i^* + \sum_s \delta m_{is}^{**} \right)^{t \rightarrow t+\Delta t} . \tag{27}$$

Finally, the particle position is moved to the new barycenter of the associated cuboid through

$$\vec{\delta x}_i = \frac{\vec{n}_s}{2 \rho_i A_i} \left(\delta m_i^* - \sum_s \delta m_{is}^{**} \right) . \tag{28}$$

This position shift ensures that a particle stays in contact with the coupled boundary until its mass reaches either zero and the particle is deleted, or the nominal particle mass and the particle is released into the domain as it is no longer eligible for mass change.

3.2. Determination of the boundary state

The coupling conditions of the two domains are defined through the state of two separate entities: ghost particles and boundary segments. As there is no overlap, the SPH domain is extended by static ghost particles to provide full kernel support of the boundary. It should be noted that this extension does not constitute an overlap, as the governing equations are not solved for these ghost particles. Instead, their state is interpolated from the VoF solution at the beginning of every SPH time iteration. Presently, we employ the *interpolationCellPoint* functionality in *OpenFOAM*, which linearly interpolates the flow fields at the position of every ghost particle from the vertices of the encompassing FV cell.

After interpolating the state of the ghost particles from the VoF domain, information about the flow on both sides of the coupled boundary is available in the SPH solver. Consequently, the state of the individual boundary segments can be determined exclusively within the SPH solver. Far from the fluid interface $\partial\chi$, or in case of a continuous field ϕ, the value at the boundary segments can be approximated through Shepard-interpolation as

$$\phi_s = \frac{\sum_j \phi_j V_j W_{sj}}{\sum_j V_j W_{sj}} . \tag{29}$$

For fields that are discontinuous across the fluid interface, the interpolation is additionally weighted with the volume fraction of the boundary segment:

$$\phi_s = \frac{\sum_{j \in \chi} \alpha_{s,\chi} \phi_j V_j W_{sj} + \sum_{j \notin \chi} \left(1 - \alpha_{s,\chi}\right) \phi_j V_j W_{sj}}{\sum_{j \in \chi} \alpha_{s,\chi} V_j W_{sj} + \sum_{j \notin \chi} \left(1 - \alpha_{s,\chi}\right) V_j W_{sj}} . \tag{30}$$

Note that the ghost particles in the interface region possess a volume fraction $0 < \alpha_{g,\chi} < 1$ and are not exclusively associated with either fluid. For the sake of simplicity, we assume that a ghost particle belongs to fluid χ if $\alpha_{g,\chi} > 0.5$.

In the present work, the formulation in Eq. (30) is only used for the pressure field in cases with surface tension to account for the pressure jump, otherwise Eq. (29) is used for both pressure and velocity fields. However, in a case where different fluids exhibit significantly differing velocity fields, the use of Eq. (30) might also be advantageous for interpolating the velocity field, for example, if a slow moving liquid is surrounded by a fast moving gas.

In addition to the pressure and velocity fields, the coupling conditions are completed by the volume fraction. Far from the fluid interface every discretization element, particle, cell, or boundary segment, is discretely associated with a single fluid and consequently the volume fraction $\alpha_{s,\chi}$ is trivially either 0 or 1. However, in the vicinity of the interface additional considerations are necessary. Here, the volume fraction in the VoF domain is non-discrete whereas SPH particles are of course associated only with a single fluid. In order to determine the volume fraction of a boundary segment, it is therefore advantageous to differentiate between the direction of flow given by the sign of the boundary normal velocity $u_{s,\perp} = \vec{u}_s \cdot \vec{n}_s$.

If the flow is directed from SPH to VoF domain, i.e. $u_{s,\perp} > 0$, the volume fraction of a boundary segment can be approximated as the ratio of the weights of the associated boundary particles:

$$\alpha^*_{s,\chi} = \frac{\sum_{j\in\chi} \omega_{js}}{\sum_j \omega_{js}}, \qquad \text{for all } s \in \partial\Omega \text{ with } u_{s,\perp} > 0. \tag{31}$$

Conversely, if the flow is directed from VoF to SPH domain, i.e. $u_{s,\perp} < 0$, the volume fraction of the boundary segment can be approximated through constant extrapolation to match that of the neighboring upwind ghost particle $g \in \mathcal{G}$:

$$\alpha^*_{s,\chi} = \alpha_{g,\chi}, \qquad \text{for all } s \in \partial\Omega \text{ with } u_{s,\perp} < 0. \tag{32}$$

This differentiation between in- and outflow regions is very convenient when they are clearly delineated. However, if the boundary normal velocity oscillates around zero in the vicinity of the fluid interface, switching between Eqs. (31) and (32) indiscriminately is ill-advised. Moreover, two edge cases have to be addressed, with the first being flow parallel to the coupled boundary, i.e. $u_{s,\perp} = 0$. The second edge cases occurs when the flow is directed from SPH to VoF domain and the predicted mass based on particle advection is much smaller than the nominal mass flux over the boundary, i.e. $u_{s,\perp} > 0$ with $\sum_j \omega_{js}\delta m^*_j \ll \Delta m_s$. This condition can persist for a few time iterations for instance if a boundary segment s is not in contact with a boundary particle or only associated with boundary particles j with a weight $\omega_{js} \ll 1$. In this case, the prediction of the volume fraction according to Eq. (31) is based on insufficient information and hence not reliable. Therefore, we propose to evolve the volume fraction in an under-relaxed formulation as

$$\alpha^{t+\Delta t}_{s,\chi} = \left(1 - \omega_{\alpha,s}\right) \alpha^t_{s,\chi} + \omega_{\alpha,s}\alpha^*_{s,\chi} \,. \tag{33}$$

The relaxation factor $\omega_{\alpha,s}$ is calculated depending on the direction of flow as

$$\omega_{\alpha,s} = 0 \leq \left[\begin{cases} \dfrac{\sum_j \omega_{js}\delta m^*_j/\rho_j}{\Delta m_s/\rho_s} & \text{if } u_{s,\perp} \geq 0 \\ \dfrac{|u_{s,\perp}|}{\eta_\omega U_{\text{char}}} & \text{if } u_{s,\perp} < 0 \end{cases} \right] \leq 1 \,. \tag{34}$$

This determination of $\omega_{\alpha,s}$ is based on heuristic considerations: For $u_{s,\perp} \geq 0$, the information contained in the weights ω_{is} is less reliable if the particle mass advected over a boundary segment is much smaller than the nominal mass Δm_s, compared to a larger ratio. Conversely, for $u_{s,\perp} < 0$, the upwind extrapolation from the VoF domain is more justified if the magnitude $|u_{s,\perp}|$ is large compared to some characteristic velocity, which is this work we set to $U_{\text{char}} = \frac{dx}{2\Delta t}$ with the additional parameter $\eta_\omega = 0.1$. However, this choice is not universal and may need to be adapted depending on the observed problem, e.g. for turbulent flow.

3.3. Preserving the discrete fluid interface

The procedure described in the previous section is sufficient to facilitate interface advection from SPH to VoF domain as the fluid interface transitions from a discrete to a continuous representation. However, if the flow is reversed, the fluid interface has to transition from a continuous representation to a discrete one. In practice, this means that particle mass of different fluids must be created on either side of the discrete fluid interface. Therefore, a simple application of the mass flow algorithm is not sufficient as it would cause particles of both fluids to be interspersed within the transition band $0 < \alpha_s < 1$. This problem is schematically illustrated in Fig. 4(a). A similar issue motivated the interface reconstruction scheme in the multi-resolution coupling of Ref. [24]. Unlike that work, our coupling approach does not include an overlap region, necessitating a related but distinct strategy to alleviate the problem.

As a first measure, we add a simple interface reconstruction procedure to the mass flux algorithm, illustrated in Fig. 4(b). The core idea is to redistribute the mass imbalance $\mathcal{M}$ between segments, so that particle mass is created on the correct side of the discrete fluid interface whenever possible. As this is only relevant if additional mass is created, the reconstruction is only applied to segments with a mass imbalance $\mathcal{M}_s > 0$. We know that the discrete fluid interface, represented by $\alpha_\chi = 0.5$, must intersect the boundary between two segments k and l for which $\alpha_{k,\chi} > 0.5$ and $\alpha_{l,\chi} < 0.5$. Consequently, we try to redistribute the imbalance

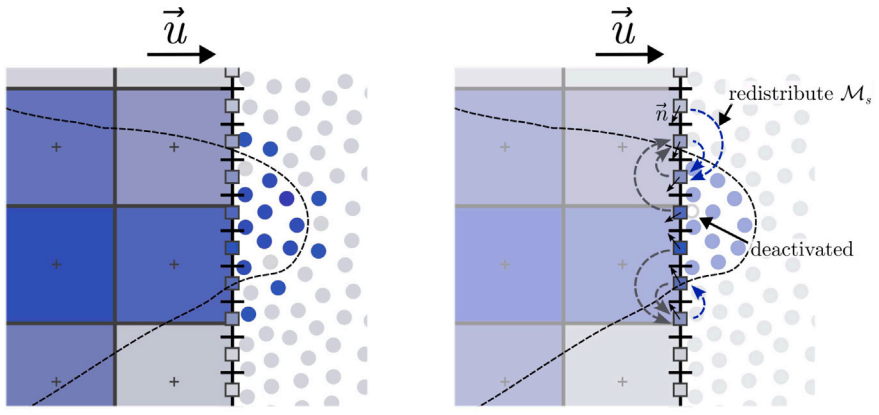

(a) Without reconstruction (b) With reconstruction

Fig. 4. Transition from a continuous to a discrete fluid interface.

$\mathcal{M}_{s,\chi}$ of a segment s with $\alpha_{s,\chi} < 0.5$ to the closest segment k with $\alpha_{k,\chi} > 0.5$. For the identification of this segment k we require a smoothed gradient of the volume fraction $\tilde{\vec{\nabla}}\alpha_{s,\chi}$, approximated as

$$\tilde{\vec{\nabla}}\alpha_{s,\chi} = \frac{\sum_k \vec{\nabla}\alpha_{k,\chi} dx^d W_{sk}}{\sum_k dx^d W_{sk}} , \tag{35}$$

$$\vec{\nabla}\alpha_{s,\chi} = \sum_j \left(\alpha_{j,\chi} - \alpha_{s,\chi}\right) V_j \vec{\nabla} W_{sj} . \tag{36}$$

The additional smoothing is necessary to ensure that the approximated gradient is directed towards fluid χ, avoiding the issue of erroneous interface normal vectors in the periphery of the interface region [32]. The segment k is then identified as $k = \arg\min_k \|\vec{x}_s - \vec{x}_k\|$ for which

$$\frac{\tilde{\vec{\nabla}}\alpha_{s,\chi} \cdot \tilde{\vec{\nabla}}\alpha_{k,\chi}}{\|\tilde{\vec{\nabla}}\alpha_{s,\chi}\|\|\tilde{\vec{\nabla}}\alpha_{k,\chi}\|} \geq \eta_\alpha , \tag{37}$$

$$\frac{\tilde{\vec{\nabla}}\alpha_{s,\chi} \cdot \vec{x}_{ks}}{\|\tilde{\vec{\nabla}}\alpha_{s,\chi}\| x_{ks}} \geq \eta_x . \tag{38}$$

Preliminary tests have revealed that $\eta_\alpha = \eta_x = 0.1$ are suitable thresholds.

Despite this interface reconstruction, a boundary particle may be 'trapped' within the other fluid, if the reconstruction fails and a particle is created within the other fluid. Moreover, even a boundary particle that has been created in the correct fluid may become 'trapped' if the interface is advected approximately perpendicular to the coupled boundary. In that case, it can occur that the fluid interface crosses the coupled boundary before the boundary particle reaches the nominal particle mass. As boundary particles are only released from the coupled boundary by the mass flux algorithm once they reach the nominal particle mass, this may result in a particle encapsulated by the other fluid. To avoid adverse effects, these 'trapped' particles are identified and 'deactivated' as depicted in Fig. 4(b). When a particle is deactivated, it is no longer considered in the quadratures and subsequently only advected parallel to the coupled boundary (denoted with the subscript $\|$) with the transport velocity $\vec{u} = \vec{\delta u}'_\|$. The shifting velocity $\vec{\delta u}'_\|$ is computed unilaterally, i.e. regular particles cause a shifting of the deactivated boundary particles, but not vice versa.

It should be noted, that the described mechanisms are solely intended to avoid dispersion of the fluid interface at the coupled boundary as it transitions from VoF to SPH domain. Additional effects on the shape of the fluid interface are both unwanted and, as demonstrated in Appendix, minimal.

3.4. Modeling of surface tension in vicinity of the coupled boundary

Both SPH and VoF employ a CSF model [20] for computing the surface tension forces in which the computation of the curvature κ is well known to be crucial [33]. In order to ensure an accurate approximation of κ close to the coupled boundary, the interface normal vector $\vec{n}$ is needed as an additional coupling condition, both for the ghost particles as well as the boundary segments. The normal vector of the ghost particles $\vec{n}_g$ can be interpolated using the same linear interpolation method as for the other coupling conditions. The normal vector of the boundary segments $\vec{n}_s$ can then be approximated according to Eqs. (9) and (36). However, this in itself is not sufficient and some modifications to the computation of surface tension forces are necessary on both sides of the coupled boundary.

3.4.1. Volume-of-fluid

Regarding the VoF domain, the interface normal vector $\vec{n}_s$ is set as a boundary condition exclusively for the approximation of the curvature based on the RDF as described in Section 2.2. Intuitively, one might replace the value of $\vec{n}_\Phi$ with $\vec{n}_s$ on the coupled cell faces before computing the curvature according to Eq. (19), however this can lead to very large curvature values in the cells adjacent to the coupled boundary, compromising both stability and accuracy of the coupled simulation. A more robust approach is to set $\vec{n}_\Phi = \vec{n}$ at the cell centers before interpolating to the face centers and computing the curvature.

3.4.2. SPH

While the modifications to the VoF surface tension model are minor, the necessary changes in the SPH methodology are more pronounced. Adami et al. [21] propose to compute the volume fraction gradient according to Eq. (8) with

$$f_{ij}^{\sigma} = \left(V_i^2 + V_j^2\right) \tilde{c}_{ij} \,. \tag{39}$$

In their approach, $\tilde{c}_{ij}$ is a density-weighted factor, distributing the force so that particles of both fluids experience equal acceleration instead of equal forces. Through this, the stability of the model is increased, allowing for a larger timestep size. However, as a negative side effect, the location of the pressure jump is shifted towards the heavier fluid [21]. Consequently, if coupled to a VoF solution where this shift does not occur, an inconsistent pressure field across the boundary might lead to inadmissible instabilities. Moreover, due to mass flux algorithm, boundary particles $\mathcal{B}$ may possess a volume much smaller than the nominal volume $V_0 = dx^d$. The interaction of particles of greatly different volumes put some additional restrictions on f_{ij}^{σ}. First, the surface tension force on a particle $i \in \mathcal{B}$ and consequently f_{ij}^{σ} should go to zero if $V_i \to 0$. Second, the impact on the surface tension force on neighboring particles should also go to zero if $V_i \to 0$. A formulation for the factor f_{ij}^{σ} satisfying these restrictions can be found as

$$f_{ij}^{\sigma} = \begin{cases} \left(V_i^2 + V_j^2\right) c_{ij} & \text{if } i, j \notin \mathcal{B}, \\ 2V_i^2 c_{ij} & \text{if } i \in \mathcal{B} \wedge j \notin \mathcal{B}, \\ 2V_i^2 V_j V_0^{-1} c_{ij} & \text{if } j \in \mathcal{B}. \end{cases} \tag{40}$$

Crucially, all three cases in Eq. (40) give identical results for $V_i = V_j = V_0$.

The factor c_{ij} serves to evenly distribute the forces between particles belonging to different fluids. Considering that only ghost particles can exhibit a volume fraction $0 < \alpha < 1$, a formulation for c_{ij} can be found as

$$c_{ij} = \left[\alpha_{i,\chi}\left(1 - \alpha_{j,\chi}\right) + \left(1 - \alpha_{i,\chi}\right)\alpha_{j,\chi}\right] \frac{\rho_i}{\rho_i + \rho_j}. \tag{41}$$

It should be noted that with the equal forces, the time step criterion (17) has to be strictly adhered to. Compared to the original formulation by Adami et al. [21], in which the criterion can be relaxed for non-unity density ratios between fluids, this can result in smaller time steps and hence higher computational cost.

Eqs. (40) and (41) are sufficient to close the surface tension model (7)–(10), but preliminary tests have shown that additional smoothing of both $\vec{n}$ and κ is advisable near the boundary, as it reduces destabilizing perturbations due to errors in the surface tension computation. Therefore, κ_i and $\vec{n}_i$ are replaced for particles with $\|\vec{x}_i - \partial\Omega\| \leq H$ by

$$\vec{\tilde{n}}_i = \frac{\sum_j \vec{n}_j V_j W_{ij}}{\sum_j V_j W_{ij}} \qquad \text{for all } j \text{ with } \|\vec{\nabla}\alpha_j\| > 0 \,, \tag{42}$$

$$\tilde{\kappa}_i = \frac{\sum_j \kappa_j V_j W_{ij}}{\sum_j V_j W_{ij}} \qquad \text{for all } j \text{ with } \|\vec{\nabla}\alpha_j\| > 0 \,. \tag{43}$$

Despite these modifications, some local deviations in the curvature approximation of neighboring particles due to particle disorder remain unavoidable. These deviations result in pressure fluctuations and, consequently, locally high pressure gradients. As the level of particle disorder is generally higher in the vicinity of the coupled boundary, the shifting velocity is also elevated in that region. When these phenomena concur, the shifting correction term in the continuity Eq. (3) may induce instabilities. To mitigate this risk, we omit the term for particles located within a distance of $\|\vec{x}_i - \partial\Omega\| \leq H$ from the coupled boundary.

3.5. Temporal coupling

In general, the two solvers use different time integration schemes with different stability regimes. While the SPH solver performs explicit time integration, the VoF solver uses an implicit scheme. Consequently, while the state of the ghost particles $\vec{X}_g^t$ is simply interpolated at the beginning of each SPH time iteration, the state of the boundary segments $\vec{X}_s^{t+\Delta t}$ must be known prior to the VoF step $t \to t + \Delta t$. Presently, this is handled through a consecutive solution of SPH and VoF equations with identical time steps, as illustrated in Fig. 5. The development of a simultaneous solution algorithm with different time step sizes is left for future work.

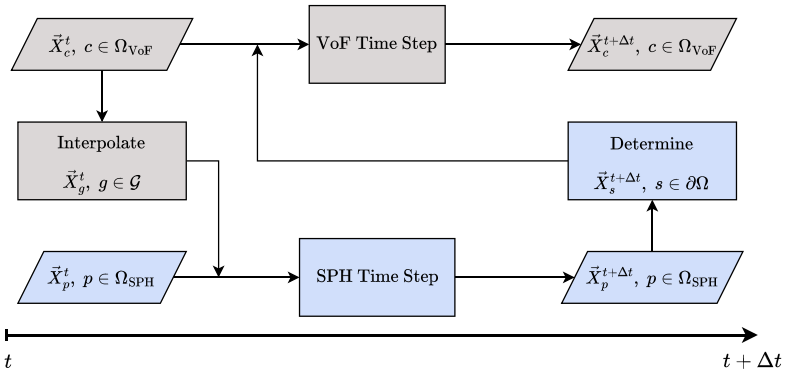

Fig. 5. Temporal coupling scheme.

4. Validation

The proposed coupling approach is validated against a series of benchmark cases, comparing it with both uncoupled SPH and FV simulations, as well as analytical solutions if available. From case to case, additional phenomena are included, starting with the single-phase Taylor–Green vortex in Section 4.1. Interfacial flows are first considered in the Kelvin–Helmholtz instability test case in Section 4.2 and extended to fluids of moderately different densities with the Rayleigh–Taylor instability in Section 4.3. Finally, the handling of surface tension effects as well as large density ratios are investigated through the advection of an oscillating droplet in Section 4.4. It should be noted that the domain decomposition, i.e. the location of the coupled boundaries, is selected to evaluate the coupling method in challenging configurations and not representative of a realistic application.

4.1. Taylor–Green vortex

Following Oger et al. [15], the Taylor–Green vortex is initialized in a square domain with $x \in [0, L]$ and $y \in [0, L]$. The analytical solution for incompressible flow is given by

$$u_x^* = \sin(2\pi x^*)\cos(2\pi y^*)\exp\left(-8\pi^2 t^*/Re\right), \tag{44}$$

$$u_y^* = -\cos(2\pi x^*)\sin(2\pi y^*)\exp\left(-8\pi^2 t^*/Re\right), \tag{45}$$

$$p^* = \frac{1}{2}\left[\cos(4\pi x^*) + \cos(4\pi y^*)\right]\exp\left(-16\pi^2 t^*/Re\right). \tag{46}$$

The kinematic viscosity ν is chosen to result in the Reynolds number of $Re = LU/\nu = 100$, with the characteristic velocity $U = \max(\|\vec{u}(t=0)\|)$. The initial Mach number and barotropic exponent are $Ma = U/c = 0.1$ and $\gamma = 7$ and the shifting parameter is set to $\varepsilon = 0.5$. The coupled boundaries are placed horizontally at $y_1 = \frac{1}{4}L$ and $y_2 = \frac{3}{4}L$ with the FV domain Ω_{FV} encompassing $y \in [y_1, y_2]$.

The resulting vortex decay is visualized in Fig. 6 through the distribution of the velocity magnitude $\|\vec{u}\|/U$ of two coupled simulations at three different non-dimensional times tU/L. In both simulations, the FV domain Ω_{FV} is discretized with a cell size of $\Delta x = L/100$, whereas the SPH domain is discretized with a mean particle spacing of $dx = L/100$ in Fig. 6(a) and $dx = L/400$ in Fig. 6(b). Qualitatively, both simulations exhibit the expected behavior, with the stable vortices decaying at a very similar rate.

This observation holds true for the relative pressure distribution displayed in Fig. 7. Note, that in order to circumvent the pressure drift due to errors in the total volume (see e.g. Sun et al. [34]) we display the relative pressure $p - \bar{p}$ instead of the absolute pressure p.

Quantitatively, the results can be analyzed more closely through the distribution of the velocity error $\mathcal{L}_2 = \|\vec{u} - \vec{u}^*\|/U$ in Fig. 8 Again, both simulations show very similar results with the largest error at $tU/L = 0.1$ which then gradually decreases. The higher resolution of the SPH domain in Fig. 8(b) leads to a comparable decrease of the $\mathcal{L}_2$ error. Crucially, the largest errors occur in regions of higher particle anisotropy in the SPH domain and not at the coupled boundary. It can therefore be concluded that the accuracy is not limited by the coupling between the domains.

Additional insight can be gained through the divergence of the velocity field depicted in Fig. 9. Here, small disturbances near the coupled boundary are evident for all time instances. However, as the disturbances are both reduced through an increase in resolution as well as localized without apparent impact far from the coupled boundary, these disturbances are not deemed to be critical.

The total, kinetic and elastic energy in the system, E_{tot}, E_{kin} and E_{elast}, evaluated as

$$E_{\text{tot}} = E_{\text{kin}} + E_{\text{elast}}, \tag{47}$$

$$E_{\text{kin}} = \frac{1}{2}\sum_{i \in \Omega} m_i \left(\vec{u}_i \cdot \vec{u}_i\right), \tag{48}$$

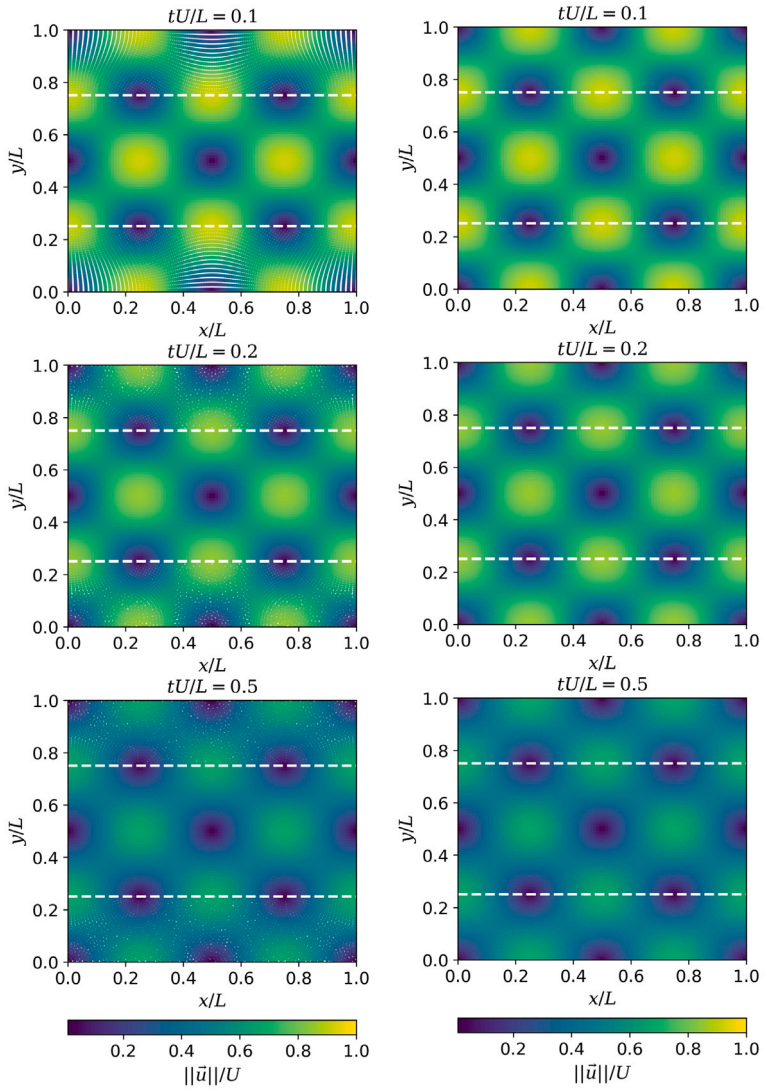

(a) $dx = \Delta x = L/100$ (b) $dx = \frac{1}{4}\Delta x = L/400$

Fig. 6. Distribution of the velocity magnitude $\| \vec{u} \|/U$ in the coupled simulations at different non-dimensional times tU/L and for different cell sizes Δx and mean particle distances dx with the white dashed lines indicating the coupled boundaries.

$$E_{\text{elast}} - E_{\text{elast},0} = \sum_{i \in \Omega} m_i \frac{c_i^2}{\gamma_i} \left(\frac{1}{\gamma_i - 1} \left[\left(\frac{\rho_i}{\rho_{0,i}} \right)^{\gamma_i - 1} - 1 \right] + \frac{\rho_{0,i}}{\rho_i} - 1 \right), \tag{49}$$

are displayed in Fig. 10. We define $E_{\text{elast},0} = E_{\text{elast}}(t = 0) = 0$ and evaluate the change in elastic energy according to [35]. Consequently, the initial total energy is given by $E_0 = E_{\text{tot},0} = E_{\text{kin},0}$. As evident from Fig. 10(a), the coupled simulations are in very good agreement with the analytical solution, while the SPH-only reference solution underpredicts the decay in kinetic energy, likely due to the non-momentum-conserving formulation for the pressure gradient (see Eq. (5)). The elastic energy depicted in Fig. 10(b), initially decays rapidly an then converges. After the initial decay, the SPH result exhibits an increase due to the errors in total volume conservation and associated pressure drift. The coupled results reveal a similar trend, however, they appear to converge towards the FV solution with increasing resolution. As a result, the total energy predicted by the coupled simulations is between that of the FV- and SPH-only simulations.

Additionally, the total mass $M = \sum_\Omega m$ within the system can be analyzed to assess whether the coupling approach causes undue errors in the conservation of mass. As evident from Fig. 11(a), the relative error $\epsilon_m = (M - M_0)/M_0$ displays an oscillating behavior with a marginal overall increase, both of which decrease with increasing resolution in the SPH domain. This convergence is confirmed by Fig. 11(b), which shows the maximum relative error depending on the mean particle spacing dx for two different

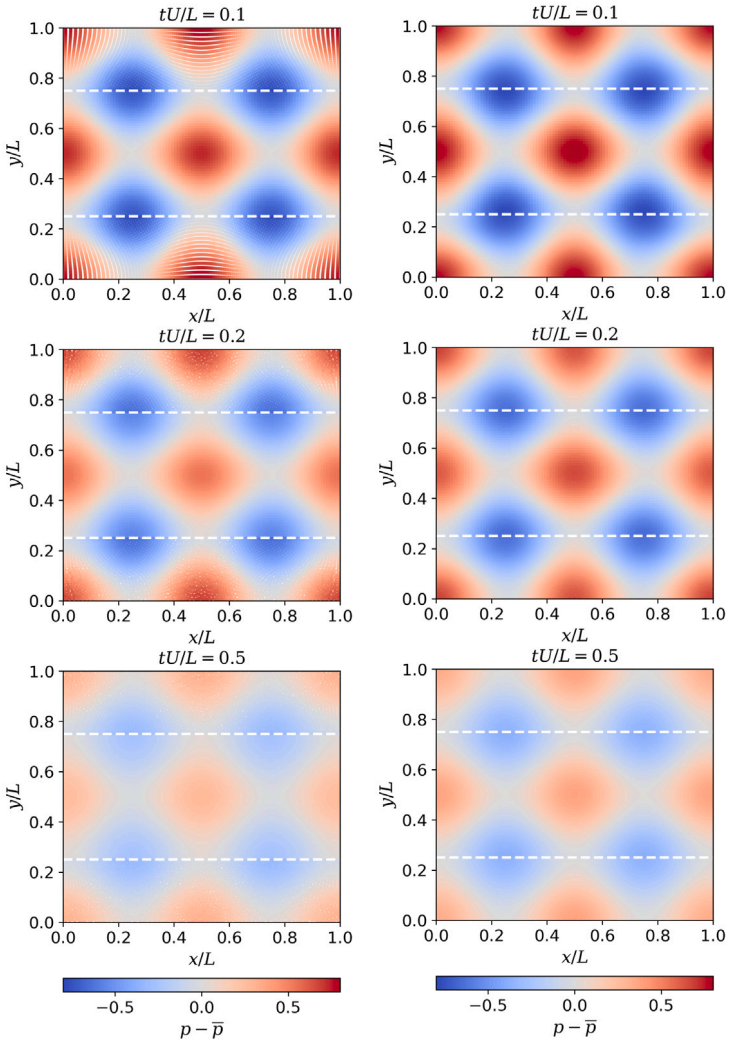

(a) $dx = \Delta x = L/100$ (b) $dx = \frac{1}{4}\Delta x = L/400$

Fig. 7. Distribution of the relative pressure $p - \overline{p}$ in the coupled simulations at different non-dimensional times tU/L and for a cell size of $\Delta x = L/100$ and different mean particle distances dx with the white dashed lines indicating the coupled boundaries.

cell sizes Δx. For the lowest resolution of $dx = \Delta x = L/100$ the maximum error is $\epsilon_m \approx 0.015\%$ and it is further reduced by increasing resolution in either domain. In fact, for a cell size of $\Delta x = L/200$, the error in coupled simulation appears to converge towards the error of a VoF-only reference solution of the same resolution, once the mean particle spacing reaches $dx = L/400$. It should be noted that while the cell size and particle spacing can in principle be varied independently, we restrict their ratio to $1 \leq \frac{\Delta x}{dx} \leq \frac{H}{dx}$.

4.2. Kelvin–Helmholtz instability

The setup of the Kelvin–Helmholtz benchmark, as illustrated in Fig. 12, is derived from Lecoanet et al. [36] with a Reynolds number of $Re = 10^4$ and a Mach number of $Ma = 0.1$. The benchmark employs a periodic domain with $x \in [0, L]$ and $y \in [-L, L]$. Initially, fluid 2 occupies the region $y \in [-\frac{1}{2}L, \frac{1}{2}L]$, while the rest of the domain is filled with fluid 1. The initial velocity components are given by

$$u_x = U\left[\tanh\left(\frac{y+\frac{1}{2}L}{a}\right) - \tanh\left(\frac{y-\frac{1}{2}L}{a}\right) - 1\right], \tag{50}$$

$$u_y = A\sin(2\pi x)\left[\exp\left(-\frac{(y+\frac{1}{2}L)^2}{b^2}\right) + \exp\left(-\frac{(y-\frac{1}{2}L)^2}{b^2}\right)\right], \tag{51}$$

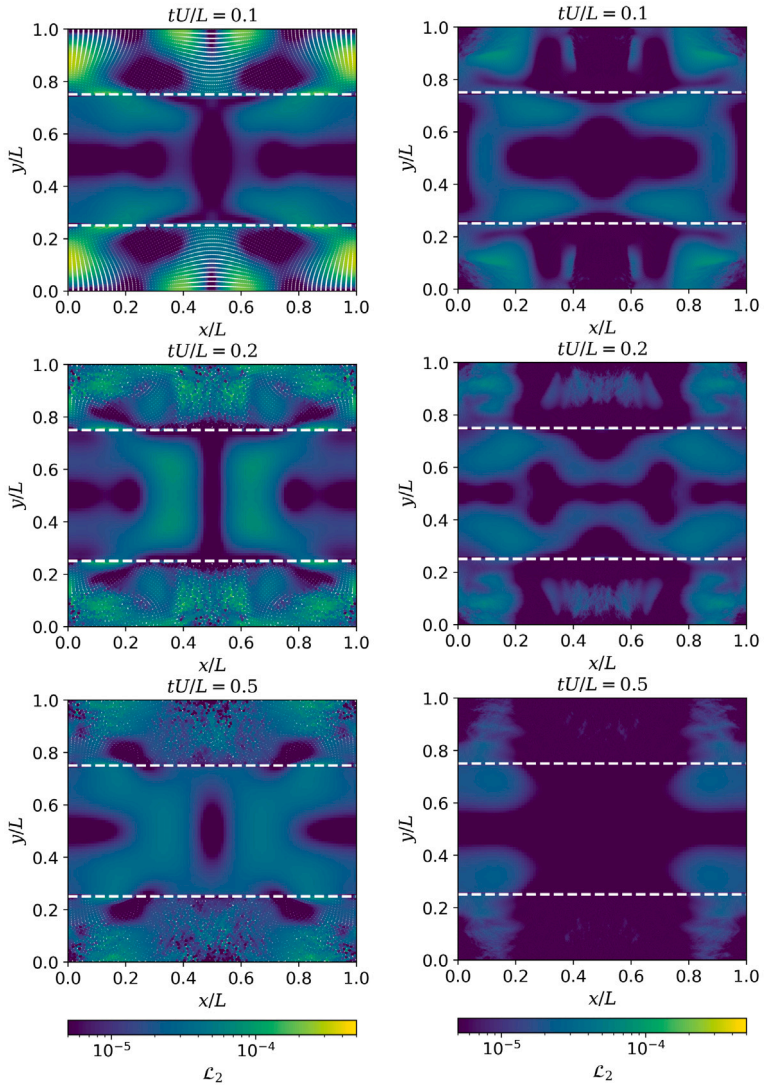

(a) $dx = \Delta x = L/100$ (b) $dx = \frac{1}{4}\Delta x = L/400$

Fig. 8. Distribution of the $\mathcal{L}_2$ velocity error in the coupled simulations at different non-dimensional times tU/L and for different cell sizes Δx and mean particle distances dx with the white dashed lines indicating the coupled boundaries.

with the bulk flow velocity $U = 1$, and the parameters $a = 0.05$ and $b = 0.2$. The instability is seeded by the initial velocity perturbation u_y with an amplitude $A = 0.05$. The barotropic exponent and shifting parameter are set to $\gamma = 7$ and $\varepsilon = 0.05$.

Two different domain decompositions are investigated: a horizontal configuration *C1* and a vertical configuration *C2*. In the horizontal configuration *C1* the coupled boundaries are located parallel to the fluid interface at $y_1 = \frac{1}{4}L$ and $y_2 = \frac{3}{4}L$, resulting in the intersection of fluid interface and coupled boundary only in the later stages of the instability growth. In the vertical configurations *C2* the coupled boundaries are situated perpendicular to the initial fluid interface at $x_1 = \frac{1}{4}L$ and $x_2 = \frac{3}{4}L$. Consequently, the fluid interface intersects the coupled boundaries during the entire simulation.

The development of the Kelvin–Helmholtz instability is visualized in Fig. 13 through snapshots of the fluid distribution of the upper half of the domain from the two coupled configurations as well as VoF- and SPH-only simulations. All displayed results are obtained with a resolution of $dx = L/400$ and $\Delta x = L/200$ in SPH and VoF domain, respectively. As is evident from these snapshots, the results from the coupled simulations are in very good agreement with their uncoupled counterparts. Even though the finest interfacial structures at the end of the simulation at $tU/L = 4$ are not perfectly resolved at the present resolution, there does not appear to be a significant impact of the coupled boundaries on the growth of the instability and the interface is advected over the domain boundary without visual disturbances.

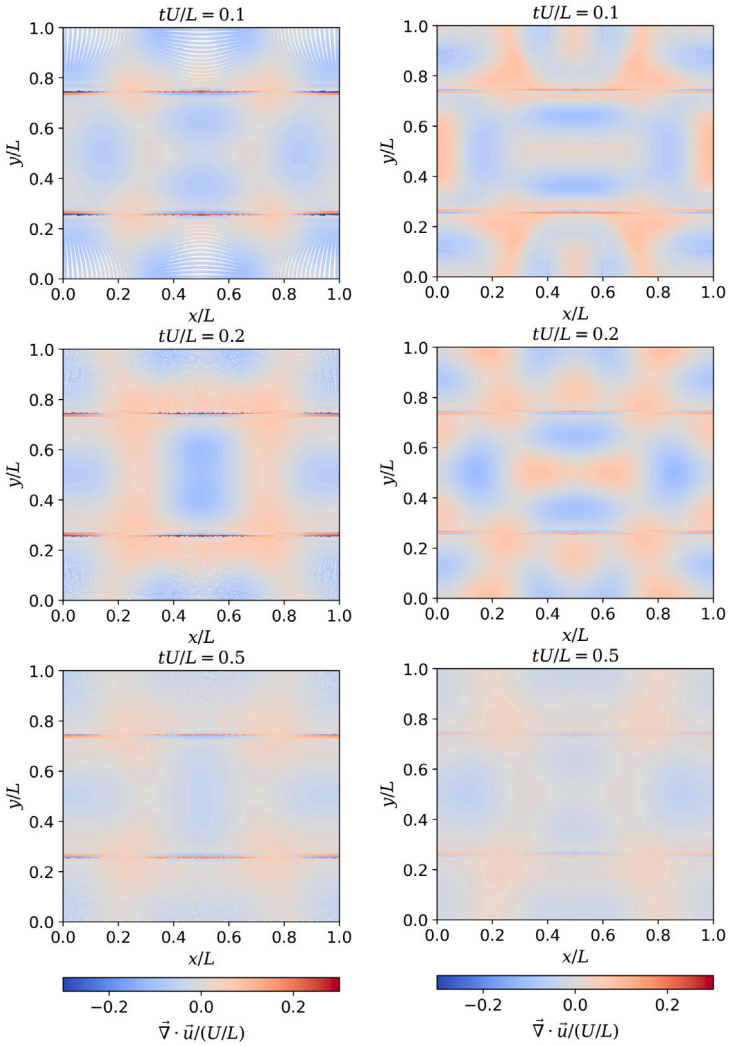

(a) $dx = \Delta x = L/100$ (b) $dx = \frac{1}{4}\Delta x = L/400$

Fig. 9. Divergence of the velocity field $\vec{\nabla} \cdot \| \vec{u} \| / (U/L)$ in the coupled simulations at different non-dimensional times tU/L and for different cell sizes Δx and mean particle distances dx.

Further insight can be gained through the plots of the fluid interface in the upper vortex core at $tU/L = 2.5$ in Fig. 14, comparing coupled simulations of varying resolution with the finest uncoupled SPH and VoF solution. For configuration *C1*, significant deviations from the finest SPH and VoF solutions can only be observed for coarsest resolution of $\Delta x = dx = L/200$. The vertical configuration *C2* in which the fluid interface intersects the coupled boundary during the entire simulation is evidently more challenging, as the reference results can only be matched for a cell size of $\Delta x = L/400$. As, however, the results of both configurations are very close to the reference results at matching resolutions, we conclude that the accuracy of the coupled approach is not significantly impeded.

In addition to the fluid interface, the vertical velocity component u_y is presented in Fig. 15 for the coarsest and finest coupled simulations and compared to the reference solutions. There is already a good agreement at the coarsest resolutions in Figs. 15(a) and 15(c), and at the finest resolutions, deviations from the reference results are comparable to the minor differences between SPH-only and VoF-only solutions.

Although the velocity field is well resolved in the coarser simulations, the divergence of the velocity field, depicted in Fig. 16, reveals disturbances in the flow field. For the horizontal coupling configuration in Fig. 16(a), these are localized to the outer cell layers of the VoF domain. In contrast, they are more pronounced on both sides of the coupled boundary in the simulation with the vertical coupling configuration in Fig. 16(c). At the higher resolution displayed in Figs. 16(b) and 16(b) however, the disturbances are greatly reduced, although they are still visible, particularly for the vertical coupling.

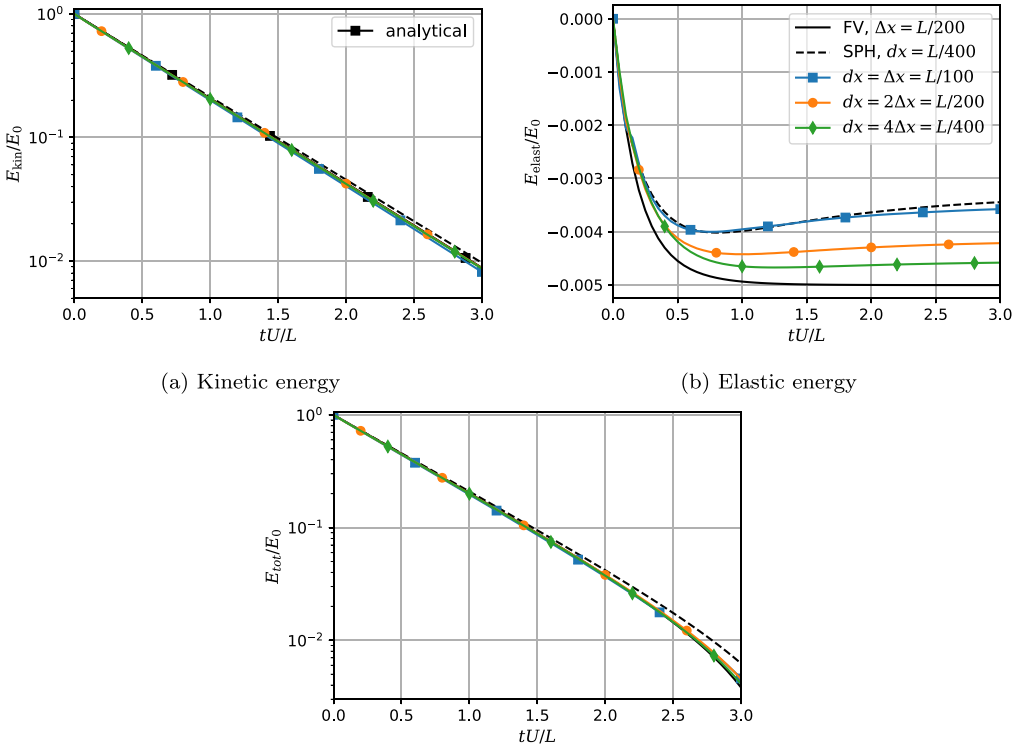

(a) Kinetic energy

(b) Elastic energy

(c) Total energy

Fig. 10. Temporal evolution of the energy components in the coupled simulations of the Taylor–Green vortex case with a cell size of $\Delta x = L/100$ compared to reference solutions.

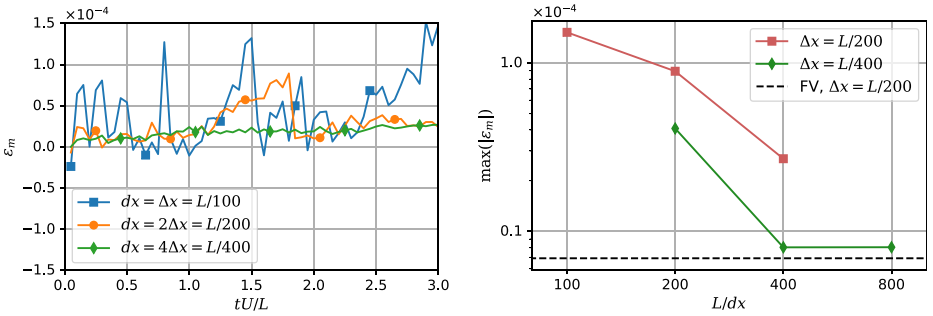

(a) Temporal evolution for $\Delta x = L/100$.

(b) Convergence of maximum error.

Fig. 11. Relative error in the conservation of mass within the domain for different discretization widths.

Analogous to Section 4.1, the relative mass error ε_m is analyzed and visualized in Fig. 17. As evident form the temporal evolution in Fig. 17(a), the two coupling configurations exhibit significantly different behavior. For the simulations employing the horizontal configuration $C1$, the error is initially very small and appears to converge with increasing resolution in the SPH domain. In the later stages of the simulations, after the fluid interface comes into contact with the coupled boundary at $tU/L \approx 3.2$, an inverse trend can be observed. Here, the increased ratio of cell size to mean particle spacing appears to cause increased error in the conservation of mass. The same trend can be observed in the results obtained with the coupling configurations $C2$. As the fluid interface intersects the coupled boundary over the entire simulated time, the increased accumulation of total mass error is evident from the start of the simulation.

As a result, the relative error is only reliably reduced by increasing resolution in the VoF domain, as evident from Fig. 17(b). The expected error reduction from increased resolution in the SPH domain is counteracted by the apparent negative impact of disparate

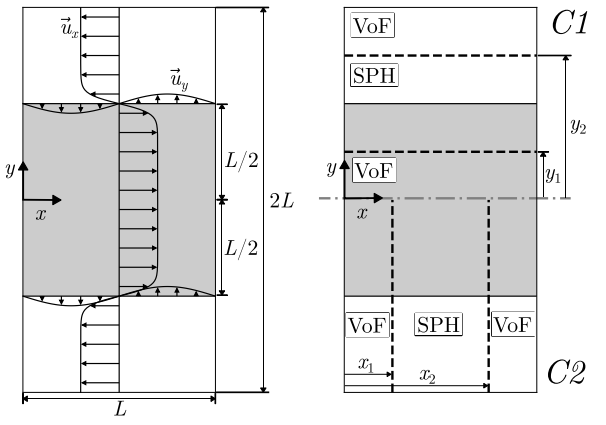

(a) Initial conditions (b) Coupling configurations

Fig. 12. Setup of the Kelvin–Helmholtz instability benchmark case.

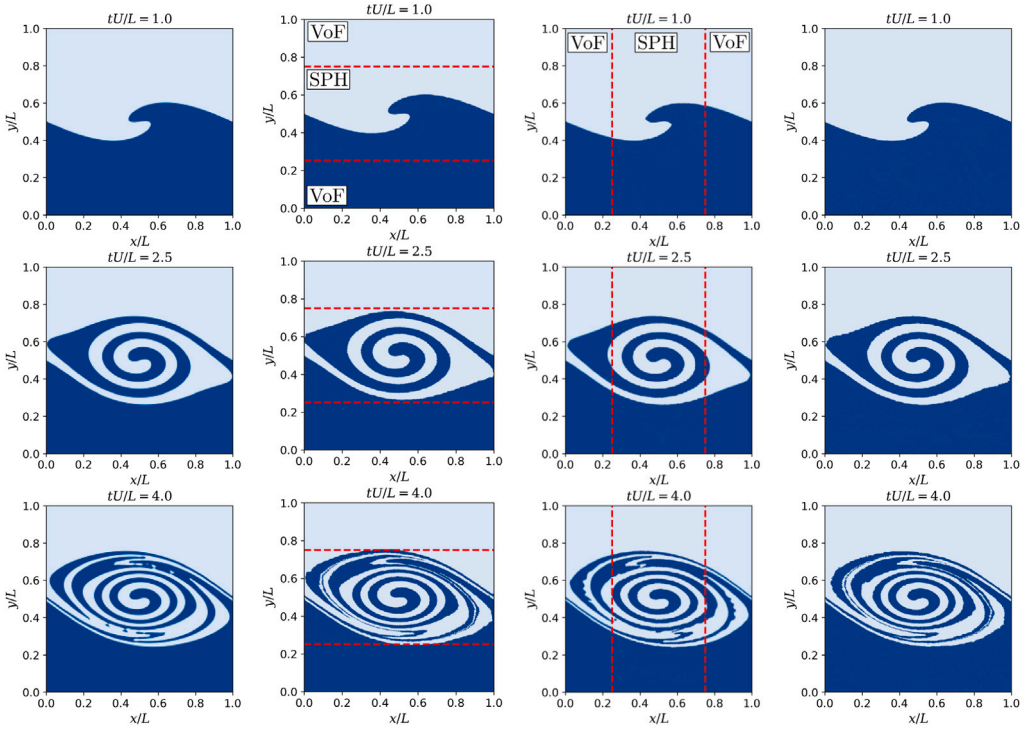

(a) VoF (b) *C1* (c) *C2* (d) SPH

Fig. 13. Snapshots of the fluid distribution during the development of the Kelvin–Helmholtz instability from the simulations with a cell size of $\Delta x = L/200$ and a mean particle spacing of $dx = L/400$ at three non-dimensional times tU/L with dashed lines indicating the coupled boundaries.

resolution of the fluid interface. However, in general, the maximum errors are still quite low, with all but one simulation showing errors below 0.1%.

4.3. Rayleigh–Taylor instability

The Rayleigh–Taylor instability is set up, as visualized Fig. 18, according to Shadloo et al. [37] in a rectangular domain with $x \in [0, L]$ and $y \in [0, 4L]$ with $L = 1\,\mathrm{m}$. The domain is enclosed by walls on which no-slip boundary conditions are enforced. Initially, the fluid interface is located at $y = 2L + 0.05L\cos\left(\frac{2\pi}{L}x\right)$ above which the domain is filled with the heavier fluid of density

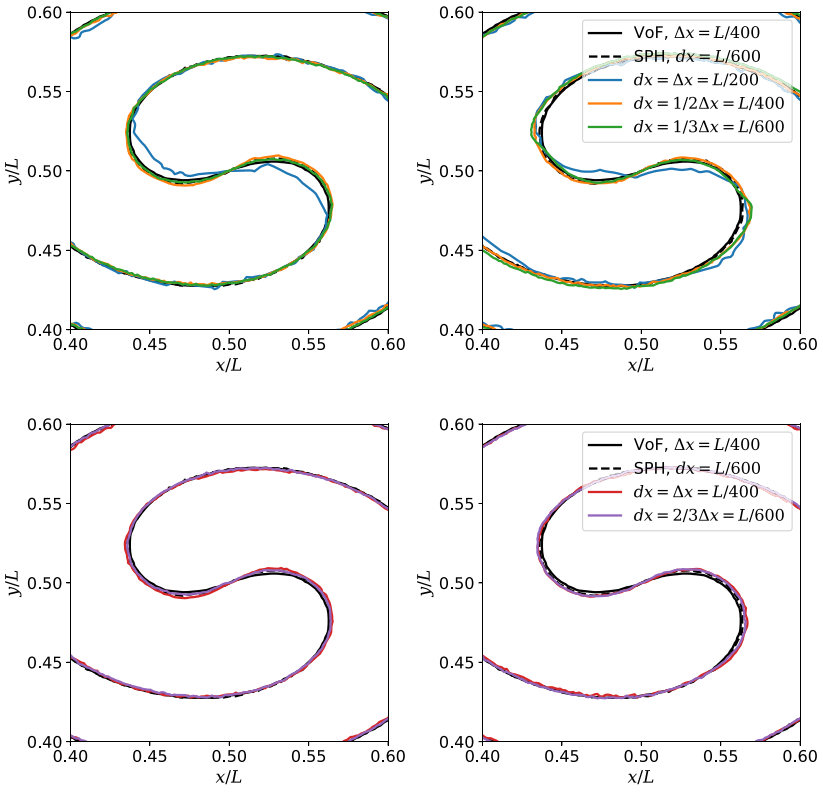

Fig. 14. Plots of the fluid interface in the upper vortex core of the Kelvin–Helmholtz instability case at $tU/L = 2.5$ for the configurations *C1* (left) and *C2* (right). The coupled results are obtained through simulations with a cell sizes of $\Delta x = L/200$ (top) and $\Delta x = L/400$ (bottom) as well as varied particle spacings dx, indicated by the color, and compared with the finest SPH and VoF simulations.

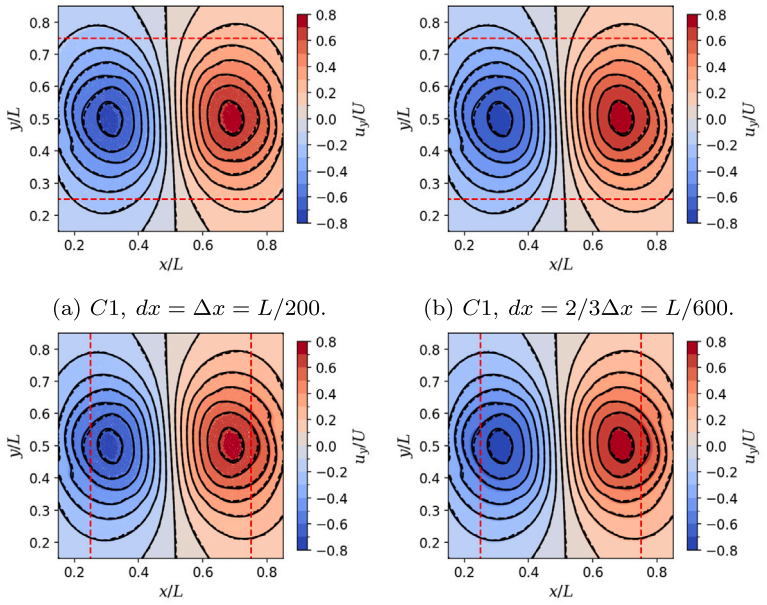

(a) $C1,\ dx = \Delta x = L/200.$ (b) $C1,\ dx = 2/3\Delta x = L/600.$

(c) $C2,\ dx = \Delta x = L/200.$ (d) $C2,\ dx = 2/3\Delta x = L/600.$

Fig. 15. Distribution of the vertical velocity component u_y of coupled simulations of the Kelvin–Helmholtz instability case in the region $x/L \in [0.15, 0.85]$ and $y/L \in [0.15, 0.85]$ at $tU/L = 2.5$ compared with the finest SPH (dashed black lines) and VoF simulations (solid black lines), with the red dashed line indicating the coupled boundary.

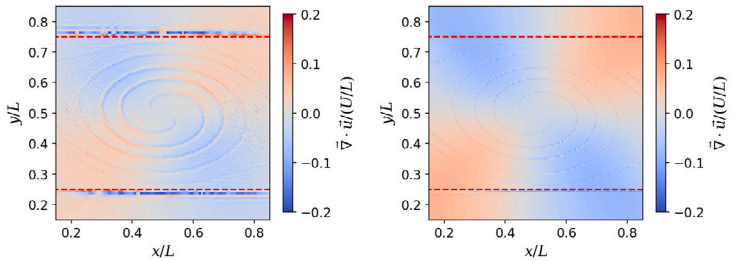

(a) $C1$, $dx = \Delta x = L/200$. (b) $C1$, $dx = 2/3\Delta x = L/600$.

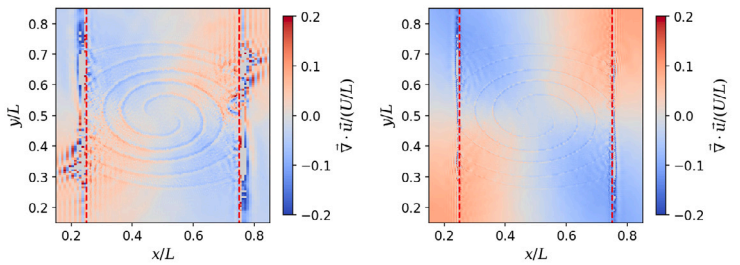

(c) $C2$, $dx = \Delta x = L/200$. (d) $C2$, $dx = 2/3\Delta x = L/600$.

Fig. 16. Divergence of the velocity field $\vec{\nabla}\cdot\vec{u}$ of coupled simulations of the Kelvin–Helmholtz instability case in the region $x/L \in [0.15, 0.85]$ and $y/L \in [0.15, 0.85]$ at $tU/L = 2.5$ with the red dashed line indicating the coupled boundary.

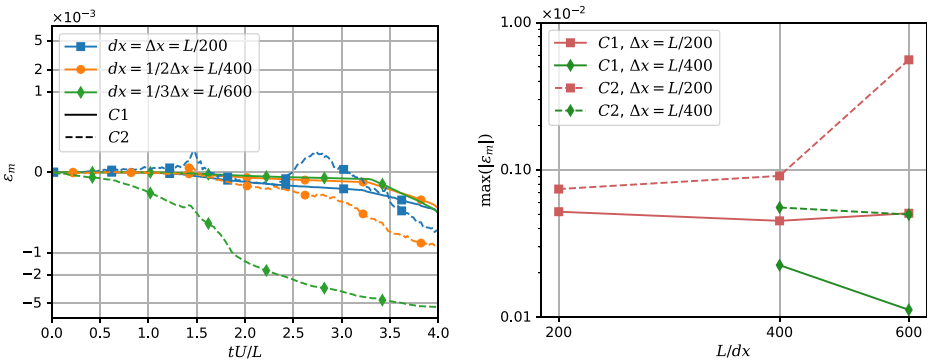

(a) Temporal evolution for $\Delta x = L/200$. (b) Convergence of maximum error.

Fig. 17. Relative error in the conservation of mass within the domain for different discretization widths.

ρ_2 =1000 kg/m^3. The density of the lighter fluid is set to ρ_1 =500 kg/m^3, resulting in an Atwood number of $At = \frac{\rho_2-\rho_1}{\rho_2+\rho_1} = \frac{1}{3}$. The kinematic viscosity of both fluids is set to $\nu_1 = \nu_2 = 1 \times 10^{-3}$ m^2/s. The instability is induced by the gravitational acceleration g_y =−0.09 m/s^2 and the surface tension is set $\sigma = 0$. Speed of sound and barotropic exponent of each fluid are set to $c_1 = 7.071$ m/s, $c_2 = 5$ m/s, and $\gamma_1 = \gamma_2 = 7$. The shifting parameter is set to $\varepsilon = 0.1$. The coupled boundary between the SPH and VoF domain is positioned below the initial fluid interface at $y_1 = 1.8L$ with the VoF domain Ω_{VoF} encompassing $y \in [0, 1.8L]$.

Fig. 19 shows snapshots of the growth of the instability from the coupled and reference simulations with $\Delta x = L/160$ and $dx = L/240$. Until the non-dimensional time $t\sqrt{g/L} = 6$, all three simulations produce virtually identical results. In the later stages, significant differences between SPH and VoF results can be observed at the present resolution with the SPH results exhibiting more chaotic disturbances to the fluid interface in the lower part of the domain. Consequently, the coupled results do not perfectly match either uncoupled simulation, although they are qualitatively closer to the VoF-only results. Overall, the coupled simulation is able to reproduce the development of the Rayleigh–Taylor of the uncoupled simulations. The remaining differences are likely caused by differences between SPH and VoF and not by the proposed coupling approach.

Again, we more closely compare the results of coupled simulations of varying resolutions with the reference solutions from the finest VoF- and SPH-only simulations with $\Delta x = L/240$ and $dx = L/320$, respectively, through the plots of the fluid interface in Fig. 20. At $t\sqrt{g/L} = 3$, only the coupled simulations with $\Delta x = L/80$ in the leftmost plot show significant differences to the reference results. All more finely resolved simulations predict a fluid interface situated between those of pure SPH and VoF. Later,

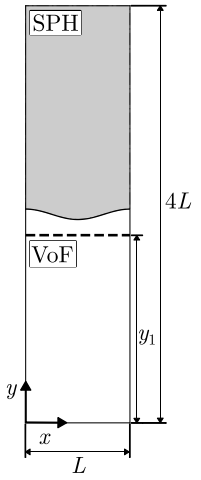

Fig. 18. Setup of the Rayleigh–Taylor instability benchmark case.

at $t\sqrt{g/L} = 4.5$ the coupled results do not converge to a solution between the SPH and VoF, however, the remaining difference is comparable to the difference between the two reference results.

In addition to the fluid distribution, the relative pressure distribution of two coupled simulations is compared to the reference results in Fig. 21. Both simulations exhibit a smooth pressure distribution over the coupled boundary. The results also show excellent agreement with the reference results, although there are some minor deviations for the coarser resolution in Fig. 21(a) at $t\sqrt{g/L} = 4.5$.

Similarly to Section 4.1, we analyze the energy in the system, with the additional potential energy component E_{pot} given by

$$E_{\text{pot}} - E_{\text{pot},0} = -g_y \sum_{i \in \Omega} m_i y_i \ . \tag{52}$$

Fig. 22 shows the temporal evolution of the energy components of the coupled simulations with a cell size of $\Delta x = L/80$ compared with the SPH- and FV-only reference solutions. As the instability grows, the potential energy decreases and the kinetic energy increases. Except for the lowest resolution, the coupled results match the reference result very well. Similarly to the Taylor–Green vortex case, both coupled and SPH-only results exhibit an increase of the elastic energy in the later stages of the simulation, most likely associated with the pressure drift due to errors in volume conservation. This error-induced increase is less pronounced with increased resolution and the elastic energy appears to converge. Consequently, the total energy predicted by the coupled simulations falls in the range given by SPH and VoF reference results for all but the lowest resolution.

4.4. Oscillating droplet

The handling of surface tension in the vicinity of the domain interface is tested through a modified version of a classical oscillating droplet benchmark case (e.g. [21]). This modified case, depicted in Fig. 23, employs a rectangular channel with $x \in [-H, H]$ and $y \in [-\frac{1}{2}H, \frac{1}{2}H]$ and the height $H = 1\,\text{m}$. SPH and VoF domain extend for $x_{\text{SPH}} \in [-H, 0]$ and $x_{\text{VoF}} \in [0, H]$ respectively. A circular droplet with the radius $R = 0.2H$ is initially located at $x_0 = -\frac{1}{2}H, y_0 = 0$ and oscillation is induced through the prescribed initial velocity field

$$u_{d,x} = -U_0 \frac{x - x_0}{r_0} \left(1 - \frac{(y - y_0)^2}{r_0 r}\right) \exp\left(-\frac{r}{r_0}\right) , \tag{53}$$

$$u_{d,y} = U_0 \frac{y - y_0}{r_0} \left(1 - \frac{(x - x_0)^2}{r_0 r}\right) \exp\left(-\frac{r}{r_0}\right) , \tag{54}$$

where $U_0 = 15\,\text{m/s}$ and $r_0 = 0.05H$. The velocity field is only prescribed for the droplet, that is for the radial coordinate $r = \sqrt{(x - x_0)^2 + (y - y_0)^2} \in [0, R)$. In addition, a frame velocity of $\overline{U}_x = 3\,\text{m/s}$ is imposed on the entire system, causing the advection of the droplet over the coupled boundary. The density and viscosity of the droplet and surrounding fluid are set to $\rho_d = 1\,\text{kg/m}^3$, $\rho_\infty = 1 \times 10^{-3}\,\text{kg/m}^3$, $\nu_d = 0.02\,\text{m}^2/\text{s}$ and $\nu_\infty = 0.2\,\text{m}^2/\text{s}$. The surface tension is varied between $0.4\,\text{N/m} \le \sigma \le 1.2\,\text{N/m}$. The speed of sound of the droplet fluid c_s is set to ensure that the density variation due to the Laplace pressure $\Delta p = \sigma/R$ does not exceed 0.5% and for the surrounding fluid to match $c_\infty = c_d \sqrt{\frac{\rho_d \gamma_\infty}{\rho_\infty \gamma_d}}$. The barotropic exponents are set $\gamma_d = 7$ and $\gamma_\infty = 1$. The shifting parameter is set to $\varepsilon = 0.1$.

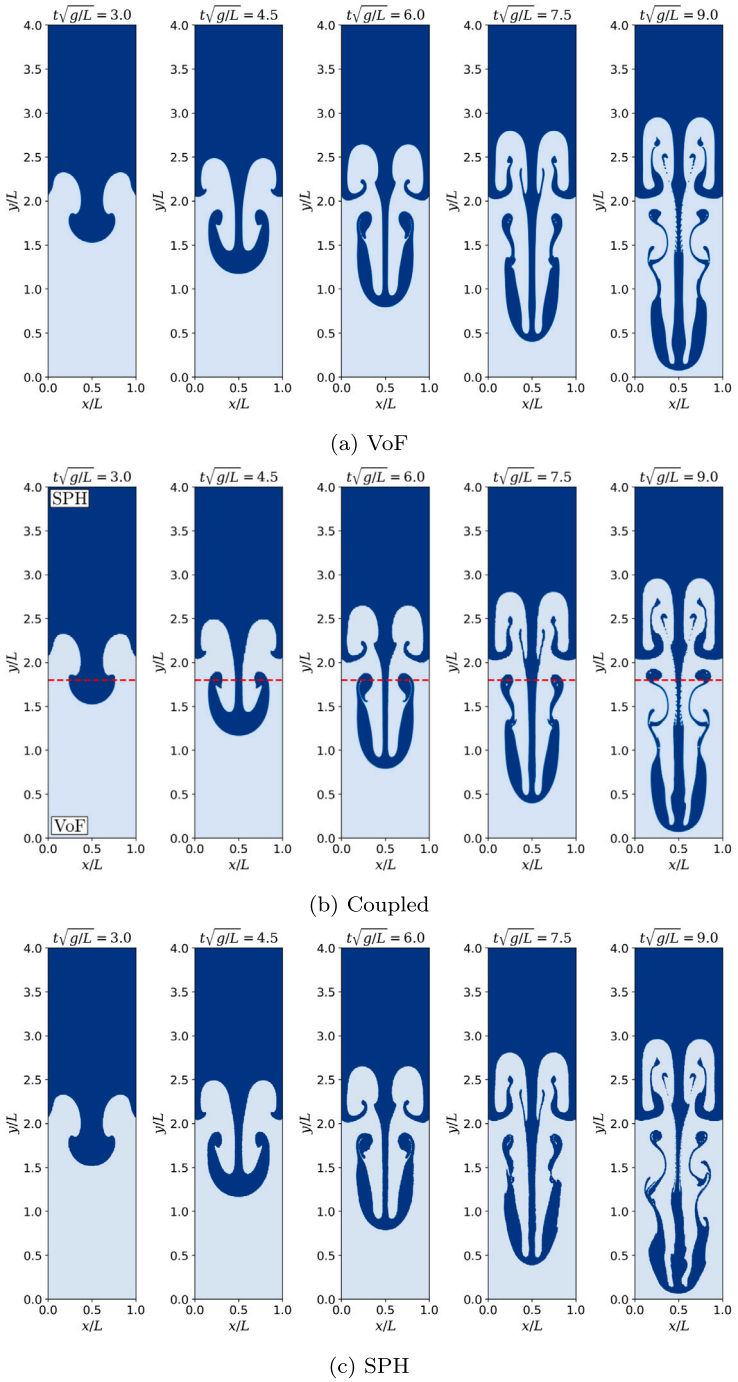

Fig. 19. Snapshots of the fluid distribution during the development of the Rayleigh–Taylor instability from the simulations with a cell size of $\Delta x = L/160$ and a mean particle spacing of $dx = L/240$ at five non-dimensional times $t\sqrt{g/L}$ with the dashed line indicating the coupled boundary.

Analogously to the previous test cases, the results of the coupled simulations with the surface tension $\sigma = 0.8\,\mathrm{N/m}$ and resolution $dx = \Delta x = H/100$ are displayed in Fig. 24 through snapshots of the fluid distribution from four time instances t, before, during and shortly after the droplet crosses the coupled boundary. There are no evident disturbances to the droplet advection and the oscillating movement continues.

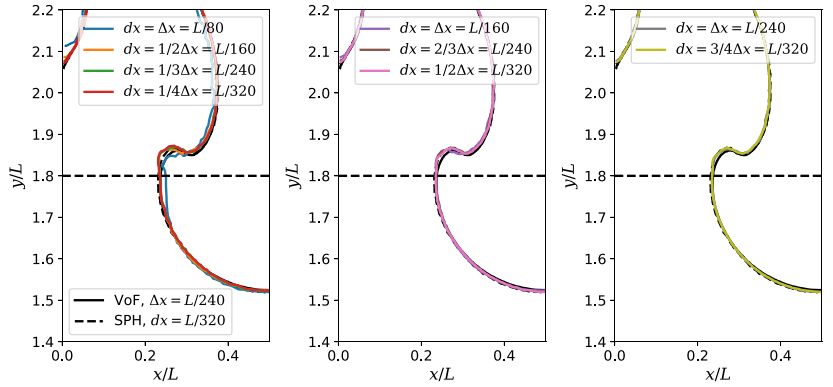

(a) $t\sqrt{g/L} = 3$

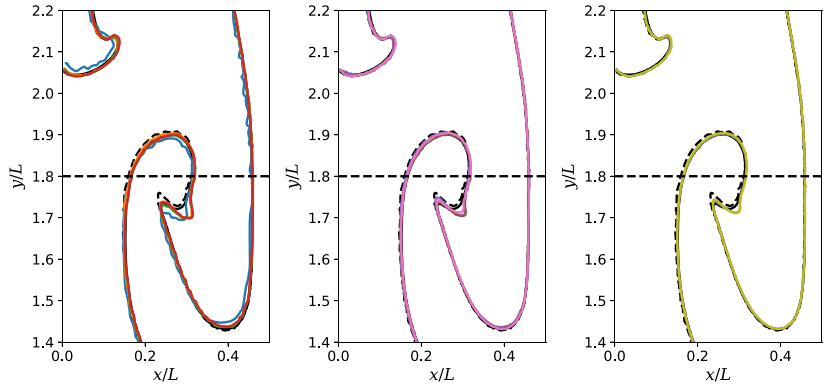

(b) $t\sqrt{g/L} = 4.5$

Fig. 20. Plots of the fluid interface of the Rayleigh–Taylor instability case in the region $x \in [0, L/2]$ and $y \in [1.4L, 2.2L]$ at two different non-dimensional times $t\sqrt{g/L}$ for cell sizes of $\Delta x = L/80$ (left), $\Delta x = L/160$ (middle) and $\Delta x = L/240$ (right) as well as varied particle spacings dx, compared with the finest SPH and VoF simulations, with the dashed line indicating the coupled boundary.

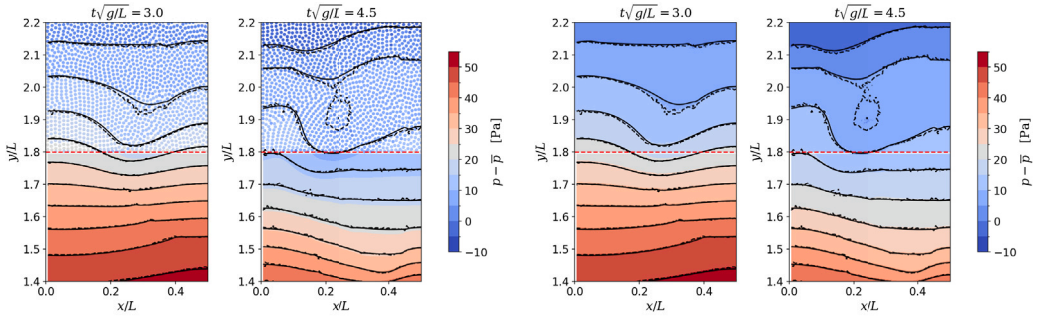

(a) $dx = \Delta x = L/80$ (b) $dx = \Delta x/4 = L/320$

Fig. 21. Distribution of the relative pressure in two coupled simulations of the Rayleigh–Taylor instability case in the region $x \in [0, L/2]$ and $y \in [1.4L, 2.2L]$ at two different non-dimensional times $t\sqrt{g/L}$ compared with the finest SPH (dashed black lines) and VoF simulations (solid black lines), with the red dashed line indicating the coupled boundary.

The oscillation behavior can be analyzed more closely through the vertical displacement of the barycenter of the top half in relation to that of the entire droplet $\Delta y = \bar{y}_{d,\text{top}} - \bar{y}_d$. This displacement is depicted in Fig. 25 for coupled simulations of varying resolution, compared to reference results from pure SPH and VoF computations. Before the droplet comes into contact with the coupled boundary (indicated by the first dashed line), the coupled results are expectedly virtually identical to the SPH-only result. Subsequently, the agreement between the coupled simulations and the SPH reference results continues to be very good, with

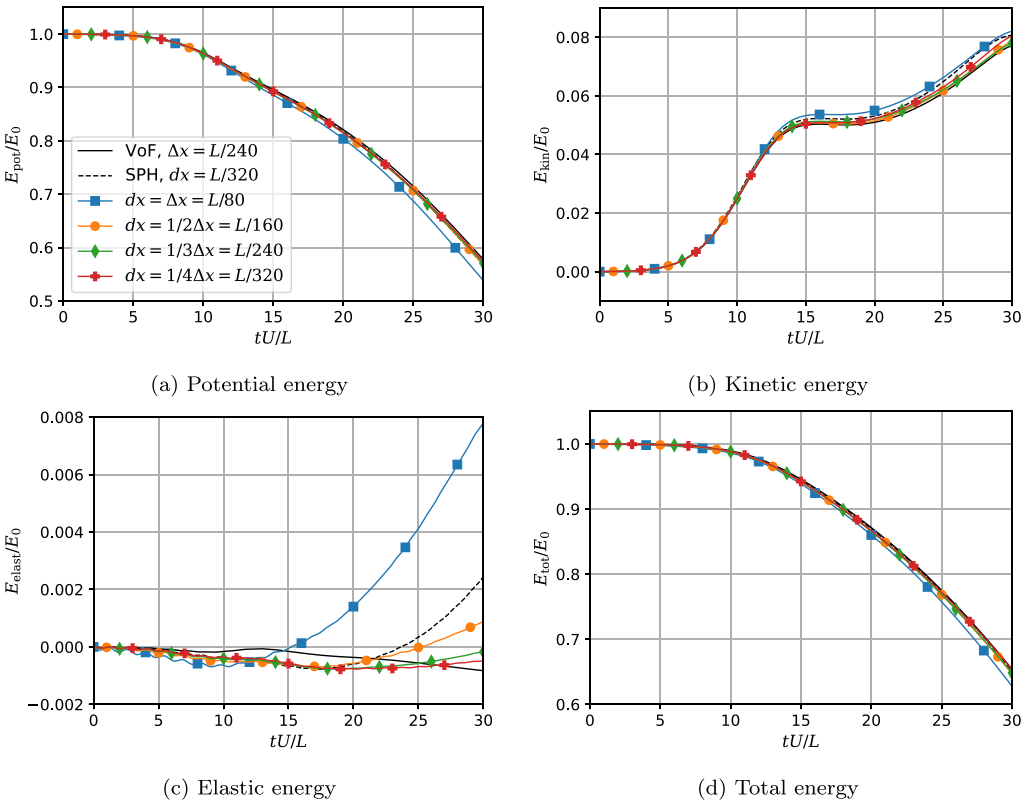

(a) Potential energy (b) Kinetic energy

(c) Elastic energy (d) Total energy

Fig. 22. Temporal evolution of the energy components in the coupled simulations of the Rayleigh–Taylor instability case with a cell size of $\Delta x = L/80$ compared to reference solutions.

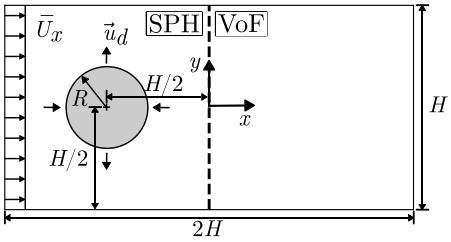

Fig. 23. Setup of the oscillating droplet benchmark case.

significant differences only evident for the coarsest coupled simulation (blue line). In fact, the deviations that do occur are smaller than those between SPH and VoF reference results. As the droplet's oscillation is undisturbed during the advection over the coupled boundary, we conclude that the proposed surface tension modeling in the vicinity of the coupled boundary works well.

Using the displacement Δy, we additionally extract the periodic time τ of the droplet oscillation over the range $0.4\,\mathrm{N/m} \leq \sigma \leq 1.2\,\mathrm{N/m}$ as shown in Fig. 26. Compared to the analytical solution $\tau_{\mathrm{ana}} = 2\pi\sqrt{R^3/6\sigma}$, all simulations overestimate the periodic time for small surface tension values. SPH and VoF reference results exhibit very similar periodic times, although VoF consistently predicts marginally higher values. All coupled SPH–VoF simulations predict values within or close to the range of the reference results, converging with increasing spatial resolution.

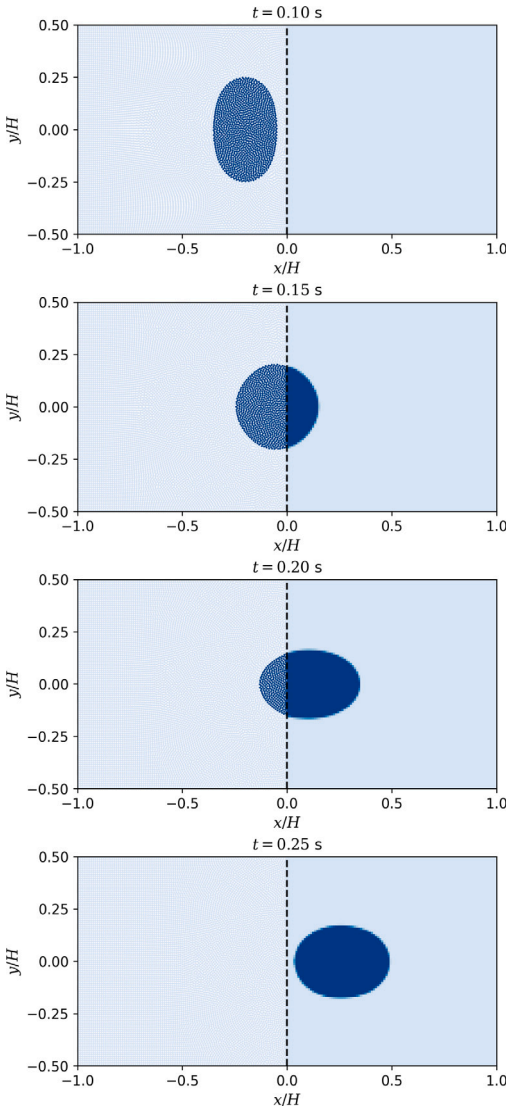

Fig. 24. Snapshots from the coupled oscillating droplet advection with $\Delta x = dx = H/100$ for various times t.

5. Conclusion

In this work, we have presented a coupled SPH–FV methodology for multiphase flow, designed to exploit the individual strengths of both methods within a patched-domain framework. Building on the approach of Werdelmann et al. [13], the proposed scheme employs the Volume-of-Fluid (VoF) method as the multiphase representation in the FV domain and is capable of interface advection over the coupled boundary. The method has been validated through a series of test cases that confront the coupling approach with the relevant physical phenomena, increasing in complexity from single-phase flow to multiphase flow with large density ratios and surface tension. To our knowledge, this is the first such method that addresses all these phenomena. It represents a significant step towards the improved modeling of complex multiphase flows through coupling of SPH and FV methods. In future work, we intend to extend this coupling to three-dimensional cases, develop a simultaneous solution algorithm, and apply the coupled method to technically relevant flows such as atomization. Apart from this, a more thorough analysis of the conservation properties of the coupled method is warranted, particularly regarding future, more complex applications, for example involving turbulence. Beyond the presented coupling method, the particle shifting scheme and specifically the repulsive interface force (RIF) term merit further investigation and detailed comparison with other multiphase particle shifting schemes.

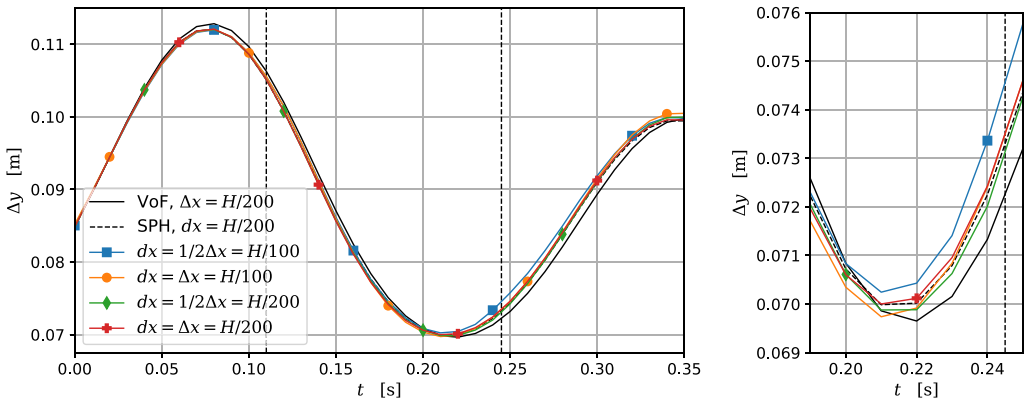

(a) $0\,\mathrm{s} \leq t \leq 0.35\,\mathrm{s}$ (b) $0.19\,\mathrm{s} \leq t \leq 0.25\,\mathrm{s}$

Fig. 25. Displacement of the barycenter of the top half of the droplet in relation to the barycenter of the entire droplet, obtained through coupled simulations of varying resolutions and compared to SPH and VoF reference result. The vertical dashed lines indicate the time during which the droplet is in contact with the coupled boundary.

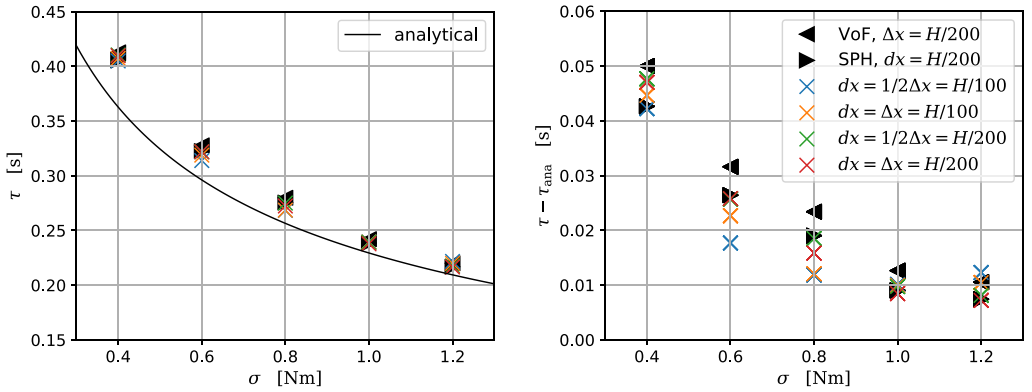

(a) Absolut value (b) Error

Fig. 26. Periodic time of the droplet oscillation, obtained through coupled simulations of varying resolutions and compared to SPH and VoF reference result as well as theory.

CRediT authorship contribution statement

Markus Wicker: Writing – original draft, Visualization, Validation, Software, Methodology, Investigation, Formal analysis, Conceptualization. **Niklas Bürkle:** Writing – review & editing, Software, Methodology. **Rainer Koch:** Writing – review & editing, Supervision, Project administration, Funding acquisition, Conceptualization. **Hans-Jörg Bauer:** Supervision, Project administration, Funding acquisition.

Declaration of competing interest

The authors declare that they have no known competing financial interests or personal relationships that could have appeared to influence the work reported in this paper.

Acknowledgments

The authors acknowledge funding by the German Federal Ministry for Economic Affairs and Energy (BMWE) within the framework of research program Luftfahrtforschungsprogramm VI-2 (Project No. 20D2102B).

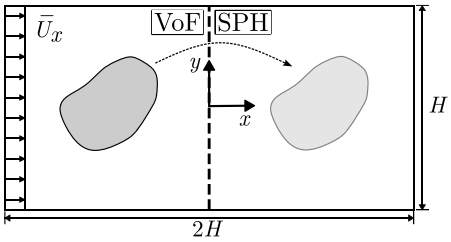

Fig. A.27. Setup of the interface advection test.

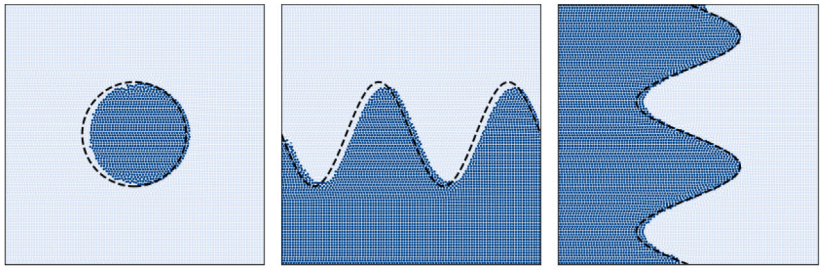

(a) $\Delta x/dx = 4$

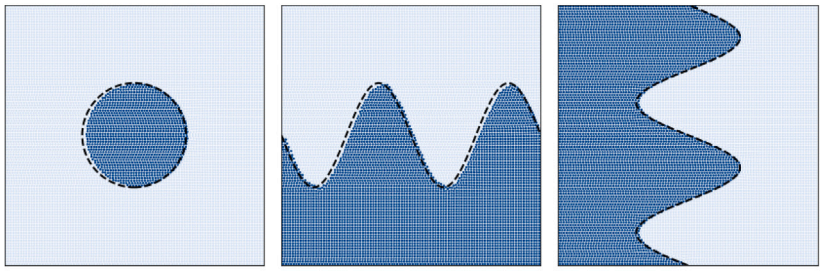

(b) $\Delta x/dx = 2$

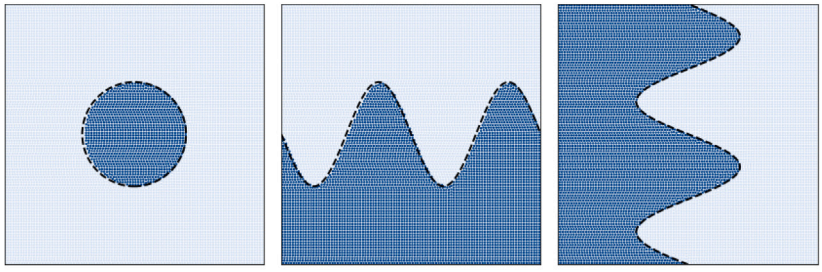

(c) $\Delta x/dx = 1$

Fig. A.28. Particle distribution in the SPH domain as result of the interface advection test for three different interface shapes compare with the exact solution (dashed line) for different ratios of cell size and particle spacing.

Appendix. Test of the interface advection

In Section 3.3, we describe the mechanisms intended to facilitate the transition from a continuous fluid interface in the VoF domain to a discrete fluid interface in the SPH domain. In order to validate these mechanisms, we set up an interface advection test as displayed in Fig. A.27. The setup consists of a rectangular domain with $x \in [-H, H]$ and $y \in [-\frac{1}{2}H, \frac{1}{2}H]$ with a coupled boundary at $x = 0$ connecting the VoF domain on the left and the SPH domain on the right. The SPH domain is discretized with a mean particle spacing of $dx = H/100$ and the cell size in the VoF domain is varied in the range $dx \leq \Delta x \leq 4dx$. Using the *setAlphaField* utility in *OpenFOAM*, different fluid interfaces are initialized in the VoF domain. A constant velocity of $\overline{U}_x = 1$ is imposed on the system, resulting in a translation of the fluid interface from VoF into SPH domain. Fig. A.28 shows the fluid interface in the SPH domain at tU/H represented by the particle distribution. For a ratio of $\Delta x/dx = 1$, the numerical results match the exact results very well

for all tested interface shapes. With an increasing ratio, the numerical results deviate from the exact solution as the fluid interface appears to be shifted marginally in positive x-direction. Nevertheless, the shape of the interface remains well preserved and there is no visible interspersion of particles of different fluids.

Data availability

Data will be made available on request.

References

[1] H.S. Tang, R.D. Haynes, G. Houzeaux, A review of domain decomposition methods for simulation of fluid flows: Concepts, algorithms, and applications, Arch. Comput. Methods Eng. 28 (3) (2021) 841–873, http://dx.doi.org/10.1007/s11831-019-09394-0.

[2] S. Marrone, A. Di Mascio, D. Le Touzé, Coupling of smoothed particle hydrodynamics with finite volume method for free-surface flows, J. Comput. Phys. 310 (2016) 161–180, http://dx.doi.org/10.1016/j.jcp.2015.11.059.

[3] B. Bouscasse, S. Marrone, A. Colagrossi, A. Di Mascio, Multi-purpose interfaces for coupling SPH with other solvers, in: Proceedings of the 8th International SPHERIC Workshop, 2013, pp. 245–252.

[4] L. Chiron, S. Marrone, A. Di Mascio, D. Le Touzé, Coupled SPH–FV method with net vorticity and mass transfer, J. Comput. Phys. 364 (2018) 111–136, http://dx.doi.org/10.1016/j.jcp.2018.02.052.

[5] A. Di Mascio, S. Marrone, A. Colagrossi, L. Chiron, D. Le Touzé, SPH–FV coupling algorithm for solving multi-scale three-dimensional free-surface flows, Appl. Ocean Res. 115 (2021) 102846, http://dx.doi.org/10.1016/j.apor.2021.102846.

[6] M.-K. Li, A.-M. Zhang, F.-R. Ming, Y.-X. Peng, A coupled smoothed particle hydrodynamics-finite volume method for three-dimensional modeling of bubble dynamics, Phys. Fluids 35 (5) (2023) 056117, http://dx.doi.org/10.1063/5.0147750.

[7] Y. Xu, G. Yang, Y. Zhu, D. Hu, A coupled SPH–FVM method for simulating incompressible interfacial flows with large density difference, Eng. Anal. Bound. Elem. 128 (2021) 227–243, http://dx.doi.org/10.1016/j.enganabound.2021.04.005.

[8] Y. Xu, G. Yang, S. Liu, D. Hu, Improvement of surface tension discrete model in the ISPH-FVM coupling method, Int. J. Multiph. Flow 160 (2023) 104347, http://dx.doi.org/10.1016/j.ijmultiphaseflow.2022.104347.

[9] Y. Xu, G. Yang, D. Hu, A three-dimensional ISPH-FVM coupling method for simulation of bubble rising in viscous stagnant liquid, Ocean Eng. 278 (2023) 114497, http://dx.doi.org/10.1016/j.oceaneng.2023.114497.

[10] Y. Xu, G. Yang, D. Hu, An enhanced mapping interpolation ISPH–FVM coupling method for simulating two-phase flows with complex interfaces, Int. J. Comput. Methods 21 (06) (2024) 2450009, http://dx.doi.org/10.1142/S0219876224500099.

[11] C. Myers, T. Palmer, C. Palmer, A hybrid Finite Volume-Smoothed Particle Hydrodynamics approach for shock capturing applications, Comput. Methods Appl. Mech. Engrg. 417 (2023) 116412, http://dx.doi.org/10.1016/j.cma.2023.116412.

[12] E. Napoli, M. De Marchis, C. Gianguzzi, B. Milici, A. Monteleone, A coupled Finite Volume–Smoothed Particle Hydrodynamics method for incompressible flows, Comput. Methods Appl. Mech. Engrg. 310 (2016) 674–693, http://dx.doi.org/10.1016/j.cma.2016.07.034.

[13] B. Werdelmann, R. Koch, W. Krebs, H.-J. Bauer, An approach for permeable boundary conditions in SPH, J. Comput. Phys. 444 (2021) 110562, http://dx.doi.org/10.1016/j.jcp.2021.110562.

[14] C. Kassiotis, D. Violeau, M. Ferrand, Semi-analytical conditions for open boundaries in smoothed particle hydrodynamics, in: Proceedings of 8th International SPHERIC Workshop, Paper, 2013, pp. 1–4.

[15] G. Oger, S. Marrone, D. Le Touzé, M. Leffe, SPH accuracy improvement through the combination of a quasi-Lagrangian shifting transport velocity and consistent ALE formalisms, J. Comput. Phys. 313 (2016) 76–98, http://dx.doi.org/10.1016/j.jcp.2016.02.039.

[16] A. Ferrari, M. Dumbser, E.F. Toro, A. Armanini, A new 3D parallel SPH scheme for free surface flows, Comput. & Fluids 38 (6) (2009) 1203–1217, http://dx.doi.org/10.1016/j.compfluid.2008.11.012.

[17] W. Dehnen, H. Aly, Improving convergence in smoothed particle hydrodynamics simulations without pairing instability, Mon. Not. R. Astron. Soc. 425 (2) (2012) 1068–1082, http://dx.doi.org/10.1111/j.1365-2966.2012.21439.x.

[18] P.N. Sun, A. Colagrossi, S. Marrone, M. Antuono, A.M. Zhang, Multi-resolution Delta-plus-SPH with tensile instability control: Towards high Reynolds number flows, Comput. Phys. Comm. 224 (2018) 63–80, http://dx.doi.org/10.1016/j.cpc.2017.11.016.

[19] K. Szewc, J. Pozorski, J.-P. Minier, Analysis of the incompressibility constraint in the smoothed particle hydrodynamics method, Internat. J. Numer. Methods Engrg. 92 (4) (2012) 343–369, http://dx.doi.org/10.1002/nme.4339.

[20] J. Brackbill, D. Kothe, C. Zemach, A continuum method for modeling surface tension, J. Comput. Phys. 100 (2) (1992) 335–354, http://dx.doi.org/10.1016/0021-9991(92)90240-Y.

[21] S. Adami, X.Y. Hu, N.A. Adams, A new surface-tension formulation for multi-phase SPH using a reproducing divergence approximation, J. Comput. Phys. 229 (13) (2010) 5011–5021, http://dx.doi.org/10.1016/j.jcp.2010.03.022.

[22] S.J. Lind, R. Xu, P.K. Stansby, B.D. Rogers, Incompressible smoothed particle hydrodynamics for free-surface flows: A generalised diffusion-based algorithm for stability and validations for impulsive flows and propagating waves, J. Comput. Phys. 231 (4) (2012) 1499–1523, http://dx.doi.org/10.1016/j.jcp.2011.10.027.

[23] N. Grenier, M. Antuono, A. Colagrossi, D. Le Touzé, B. Alessandrini, An Hamiltonian interface SPH formulation for multi-fluid and free surface flows, J. Comput. Phys. 228 (22) (2009) 8380–8393, http://dx.doi.org/10.1016/j.jcp.2009.08.009.

[24] N. Bürkle, M. Wicker, M. Okraschevski, R. Koch, H.-J. Bauer, A SPH multi-resolution framework for multi-phase flows, Comput. Methods Appl. Mech. Engrg. 449 (2026) 118505, http://dx.doi.org/10.1016/j.cma.2025.118505.

[25] A. Khayyer, H. Gotoh, Y. Shimizu, A projection-based particle method with optimized particle shifting for multiphase flows with large density ratios and discontinuous density fields, Comput. & Fluids 179 (2019) 356–371, http://dx.doi.org/10.1016/j.compfluid.2018.10.018.

[26] A.M. Xenakis, S.J. Lind, P.K. Stansby, B.D. Rogers, An incompressible smoothed particle hydrodynamics scheme for Newtonian/non-Newtonian multiphase flows including semi-analytical solutions for two-phase inelastic Poiseuille flows, Internat. J. Numer. Methods Fluids 92 (7) (2020) 703–726, http://dx.doi.org/10.1002/fld.4802.

[27] H. Scheufler, J. Roenby, TwoPhaseFlow: A framework for developing two phase flow solvers in OpenFOAM, OpenFOAM® J. 3 (2023) 200–224, http://dx.doi.org/10.51560/ofj.v3.80.

[28] J. Roenby, H. Bredmose, H. Jasak, A computational method for sharp interface advection, R. Soc. Open Sci. 3 (11) (2016) 160405, http://dx.doi.org/10.1098/rsos.160405, Publisher: Royal Society.

[29] H. Scheufler, J. Roenby, Accurate and efficient surface reconstruction from volume fraction data on general meshes, J. Comput. Phys. 383 (2019) 1–23, http://dx.doi.org/10.1016/j.jcp.2019.01.009.

[30] S.J. Cummins, M.M. Francois, D.B. Kothe, Estimating curvature from volume fractions, Comput. Struct. 83 (6) (2005) 425–434, http://dx.doi.org/10.1016/j.compstruc.2004.08.017.
[31] S. Braun, L. Wieth, S. Holz, T.F. Dauch, M.C. Keller, G. Chaussonnet, S. Gepperth, R. Koch, H.-J. Bauer, Numerical prediction of air-assisted primary atomization using Smoothed Particle Hydrodynamics, Int. J. Multiph. Flow 114 (2019) 303–315, http://dx.doi.org/10.1016/j.ijmultiphaseflow.2019.03.008.
[32] J.P. Morris, Simulating surface tension with smoothed particle hydrodynamics, Internat. J. Numer. Methods Fluids 33 (3) (2000) 333–353, http://dx.doi.org/10.1002/1097-0363(20000615)33:3<333::AID-FLD11>3.0.CO;2-7.
[33] S. Popinet, Numerical models of surface tension, Annu. Rev. Fluid Mech. 50 (2018) 49–75, http://dx.doi.org/10.1146/annurev-fluid-122316-045034.
[34] P.N. Sun, A. Colagrossi, S. Marrone, M. Antuono, A.M. Zhang, A consistent approach to particle shifting in the δ-Plus-SPH model, Comput. Methods Appl. Mech. Engrg. 348 (2019) 912–934, http://dx.doi.org/10.1016/j.cma.2019.01.045.
[35] J.J. Monaghan, A. Rafiee, A simple SPH algorithm for multi-fluid flow with high density ratios, Internat. J. Numer. Methods Fluids 71 (5) (2013) 537–561, http://dx.doi.org/10.1002/fld.3671, _eprint: https://onlinelibrary.wiley.com/doi/pdf/10.1002/fld.3671.
[36] D. Lecoanet, M. McCourt, E. Quataert, K.J. Burns, G.M. Vasil, J.S. Oishi, B.P. Brown, J.M. Stone, R.M. O'Leary, A validated non-linear Kelvin–Helmholtz benchmark for numerical hydrodynamics, Mon. Not. R. Astron. Soc. 455 (4) (2016) 4274–4288, http://dx.doi.org/10.1093/mnras/stv2564.
[37] M.S. Shadloo, A. Zainali, M. Yildiz, Simulation of single mode Rayleigh–Taylor instability by SPH method, Comput. Mech. 51 (5) (2013) 699–715, http://dx.doi.org/10.1007/s00466-012-0746-2.